

An image-based method for modeling the elasto-plastic behavior of polycrystalline microstructures based on the fast Fourier transform

Bin Wen, Nicholas Zabaras*

Materials Process Design and Control Laboratory, Sibley School of Mechanical and Aerospace Engineering, 101 Frank H.T. Rhodes Hall, Cornell University, Ithaca, NY 14853-3801, USA

Abstract

An efficient full-field method of computing the local and homogenized macroscopic responses of elasto-plastic polycrystalline microstructures based on the fast Fourier transform (FFT) algorithm is presented. This approach takes realistic microstructure images as the input and estimates the mechanical response/properties of polycrystal microstructures under periodic boundary conditions without requiring complex discretization. Effective stress-strain response, local mechanical response fields and crystallographic texture of deformed microstructures are examined. Special interest is given to the fatigue indicator parameters (FIPs) of IN100 (nickel-based superalloy). This approach accounts for both intergranular and intragranular interactions of an elasto-plastic heterogeneous medium and therefore provides accurate prediction of the mechanical response and texture evolution. The elastic and plastic responses are computed separately by satisfying two forms of the equilibrium equations. A multi-grid strategy is also adopted to capture the heterogeneous deformation of microstructures. The obtained results are compared with a widely used crystal plasticity finite element approach. The gained computational efficiency of full-field polycrystalline microstructure simulation is prominent.

Keywords:

Polycrystalline microstructure, Full-field simulation, Fast Fourier transform,

*Corresponding author: Fax: 607-255-1222, Email: nzabaras@gmail.com, URL: <http://mpdc.mae.cornell.edu/>

Report Documentation Page			Form Approved OMB No. 0704-0188		
Public reporting burden for the collection of information is estimated to average 1 hour per response, including the time for reviewing instructions, searching existing data sources, gathering and maintaining the data needed, and completing and reviewing the collection of information. Send comments regarding this burden estimate or any other aspect of this collection of information, including suggestions for reducing this burden, to Washington Headquarters Services, Directorate for Information Operations and Reports, 1215 Jefferson Davis Highway, Suite 1204, Arlington VA 22202-4302. Respondents should be aware that notwithstanding any other provision of law, no person shall be subject to a penalty for failing to comply with a collection of information if it does not display a currently valid OMB control number.					
1. REPORT DATE 16 MAR 2012		2. REPORT TYPE		3. DATES COVERED 00-00-2012 to 00-00-2012	
4. TITLE AND SUBTITLE An image-based method for modeling the elasto-plastic behavior of polycrystalline microstructures based on the fast Fourier transform				5a. CONTRACT NUMBER	
				5b. GRANT NUMBER	
				5c. PROGRAM ELEMENT NUMBER	
6. AUTHOR(S)				5d. PROJECT NUMBER	
				5e. TASK NUMBER	
				5f. WORK UNIT NUMBER	
7. PERFORMING ORGANIZATION NAME(S) AND ADDRESS(ES) Cornell University, Sibley School of Mechanical and Aerospace Engineering, Ithaca, NY, 14853				8. PERFORMING ORGANIZATION REPORT NUMBER	
9. SPONSORING/MONITORING AGENCY NAME(S) AND ADDRESS(ES)				10. SPONSOR/MONITOR'S ACRONYM(S)	
				11. SPONSOR/MONITOR'S REPORT NUMBER(S)	
12. DISTRIBUTION/AVAILABILITY STATEMENT Approved for public release; distribution unlimited					
13. SUPPLEMENTARY NOTES					
14. ABSTRACT An efficient full-field method of computing the local and homogenized macroscopic responses of elasto-plastic polycrystalline microstructures based on the fast Fourier transform (FFT) algorithm is presented. This approach takes realistic microstructure images as the input and estimates the mechanical response/properties of polycrystal microstructures under periodic boundary conditions without requiring complex discretization. Effective stress-strain response, local mechanical response fields and crystallographic texture of deformed microstructures are examined. Special interest is given to the fatigue indicator parameters (FIPs) of IN100 (nickel-based superalloy). This approach accounts for both intergranular and intragranular interactions of an elasto-plastic heterogeneous medium and therefore provides accurate prediction of the mechanical response and texture evolution. The elastic and plastic responses are computed separately by satisfying two forms of the equilibrium equations. A multi-grid strategy is also adopted to capture the heterogeneous deformation of microstructures. The obtained results are compared with a widely used crystal plasticity finite element approach. The gained computational efficiency of full-field polycrystalline microstructure simulation is prominent.					
15. SUBJECT TERMS					
16. SECURITY CLASSIFICATION OF:			17. LIMITATION OF ABSTRACT Same as Report (SAR)	18. NUMBER OF PAGES 54	19a. NAME OF RESPONSIBLE PERSON
a. REPORT unclassified	b. ABSTRACT unclassified	c. THIS PAGE unclassified			

1. Introduction

Numerical prediction of effective and local mechanical behavior of polycrystalline materials has received great attention in the computational materials science community starting with the pioneering work on crystal plasticity using physically-based models by Sachs [1] and Taylor [2]. The Sachs model, assumes that each grain in the polycrystalline aggregate is subjected to the same stress and provides lower bound prediction to the effective stress-strain response. This model was extended to deal with large visco-plastic and elasto-viscoplastic deformations and is known as the lower bound model [3]. On the other hand, the Taylor model also known as the upper bound model assumes uniform strain in the polycrystal (equal to the macroscopic value), and provides rigid prediction to the effective stress-strain response of the microstructure. Extensions of the Taylor model to elasto-plastic [4], viscoplastic [5], and finite elasto-viscoplastic deformations [6] were proposed. Although not accounting for the interactions inside the microstructure, the Taylor model has been widely used in computational crystal plasticity community for its simplicity and high computational efficiency [7, 8, 9, 10].

The above models, however, only give approximate (or more precisely, extreme) estimation of the effective mechanical behavior of polycrystalline microstructures by assuming homogeneous fields over the domain. The local mechanical response of deformed microstructures cannot be accurately captured. To account for intergranular interaction during deformation, a more sophisticated and popular homogenization strategy, self-consistent method, has been developed. The formulation of self-consistent models is based on the solution of the problem of an ellipsoidal inclusion embedded in an infinite homogeneous equivalent medium. The inclusion is taken to be an individual grain while the homogeneous medium represents the equivalent polycrystalline aggregate. Each inclusion (or grain) is taken as an averaged medium, the heterogeneity within which is not considered. The first attempt to model the overall elasto-plastic behavior of polycrystals through the self-consistent approach was proposed by Kröner [11] based on the use of Eshelby's solution [12]. This model neglects plastic interactions between the inclusion and the surrounding matrix. An improvement was introduced by Hill [13] to account for the plastic interaction using an incremental formulation based on

the linearization of the local constitutive equations. This model was later implemented for polycrystals [14]. Hill’s incremental approach, which is known as the *secant* model, was extended to study polycrystals at large elastic-plastic deformations in [15]. A non-incremental self-consistent approach by using the tangent modulus-based formulation was proposed in [16]. This work has been used to simulate large visco-plastic deformations in various crystalline materials with full anisotropic overall tangent modulus [17, 18]. These works were further extended to a general elasto-viscoplastic model in [19]. An “affine” model, which yields softer predictions, was later proposed [20, 21] to study rate-dependent elasto-plastic behavior of polycrystals. All these developments are based on linearization schemes that, at grain level, only make use of information on field averages, disregarding higher-order statistical information inside the grain. Improvements taking consideration of the second-order moment of the field fluctuation in grains were also developed in [22, 23, 24] to account for intragrain heterogeneities.

Self-consistent models are widely adopted to study the effective mechanical response and texture evolution of polycrystalline microstructures. Although they give more reliable predictions to macroscopic properties than the Sachs and Taylor models, these “mean-field” methods are still not capable of estimating local micromechanical fields appropriately since a homogeneous grain is assumed. To this end, full-field simulations that interrogate polycrystalline microstructures with intracrystalline resolution are developed with the evolution of computing power. The most popular full-field model for polycrystals nowadays is the crystal plasticity finite element method, in which a variational solution is achieved for the force equilibrium and displacement compatibility using the principle of virtual work for a domain that is discretized into finite elements. Several crystal plasticity finite element models have been developed incorporating different physics-based constitutive laws since the early work by Peirce et al. [25]. For a detailed overview, the reader is referred to [26], where theories and applications of crystal plasticity finite element models are reviewed. In our earlier work, a rate-independent constitutive model [27] along with the grain size effect described by lattice incompatibility [28] were implemented to study the mechanical response of polycrystalline FCC microstructures discretized by conforming grids [29]. A rate-dependent nickel-based superalloy constitutive model [30] was later embedded in our crystal plasticity finite element framework to study fatigue properties and their variability induced by microstructure uncertainties [31].

The difficulty in finite element meshing coupled with the large number of

degrees of freedom, however, limits the size of the microstructures that can be investigated by finite element simulations. In addition, the high computation cost of crystal plasticity finite element analysis also prevents it from being used as the deterministic solver in stochastic simulations or as a point simulator in multiscale simulations. Another efficient full-field approach based on Green's functions and fast Fourier transform (FFT) has been proposed as an alternative to the finite element method for solving the governing equations for periodic heterogeneous media [32, 33]. This fast Fourier transform-based method was originally proposed as a fast algorithm to compute the elastic and elasto-plastic effective and local response of composites with isotropic components [34, 35, 36]. This approach was also adapted to deal with polycrystalline microstructures using a visco-plastic constitutive model [32]. Local and macro mechanical responses, as well as the texture evolution, of 2D and 3D realistic polycrystals were studied in a series of works [32, 37, 38]. Comparison with the self-consistent method [39] and finite element simulations [40, 41] were conducted and showed the accuracy and efficiency of the fast Fourier transform scheme. Recent attempts to couple the fast Fourier transform-based model with finite elements is presented in [42]. The major merit of the crystal plasticity fast Fourier transform-based method lies in the following aspects:

1. It directly works on pixelized microstructure images without requiring sophisticated discretization.
2. It is a full-field method that accurately investigates the global and local mechanical behavior of microstructures by accounting for both intergrain and intragrain interactions.
3. It has better numerical performance than the crystal plasticity finite element method for the same spatial resolution without sacrificing accuracy [40].

Recent crystal plasticity fast Fourier transform models neglect elastic behavior and consider only visco-plastic constitutive behavior. For a microstructure under large plastic deformation, this approximation is valid as elastic strain is usually very small. In certain cases, however, both elastic and plastic mechanisms are important, e.g. fatigue analysis of turbine engine components under cyclic loading. Driven by this requirement, we here introduce a new fast Fourier transform-based crystal plasticity model with the incorporation of elasto-plastic constitutive relations (we call it, in abbreviation, CEPFFT). The total strain rate is additively decomposed into an elastic part

and a plastic part. The elastic and plastic responses are computed separately using the fast Fourier transform-based method and combined to update the stress field. Through a series of benchmark examples, it is shown that the effective and local mechanical responses predicted by CEPFFT are in good agreement with the crystal plasticity finite element results. A constitutive model of IN100 [30] is also employed to study the microstructure-sensitive fatigue indicator parameters of such Ni-based superalloy under cyclic loading. Comparison with finite element solutions shows great consistence of the two methods. Besides, we analyzed the performance of the fast Fourier transform based simulator with pure visco-plastic model implemented in two different ways (basic formulation and augmented Lagrangian approach). It is observed that both algorithms work equally well for crystal plasticity problems. A multi-grid strategy separating the computation and material grids based on the particle-in-cell method [43] is also employed and the obtained results are compared with those using a single grid strategy [40].

The organization of the paper is as follows. In Section 2, the formulation of CEPFFT algorithm is introduced. We start with pure elastic and visco-plastic situations and extend to elasto-plastic problem. A complete boundary value problem along with the solution strategy and elasto-plastic constitutive relation is described. Specific constitutive models that are adopted in the paper are presented in Section 3. The input model and microstructure update strategy are described in Section 4. Facts about the crystal plasticity finite element method are briefly reviewed in Section 5. Numerical examples are demonstrated in Section 6, where comparisons between the various methods for several benchmark problems are shown. Error analysis and computational efficiency tests are conducted. The multi-grid and single-grid results are also presented. Finally, a brief summary is provided in Section 7.

2. Crystal Elasto-Plastic Fast Fourier Transform Simulator

In this section, we address the solution of the boundary value problem defining the deformation of elasto-plastic polycrystalline microstructures using Green’s function method, in which any point in the domain can be considered as an inclusion embedded in a homogeneous reference medium. The local mechanical response of the heterogeneous medium can be calculated as a convolution integral between the Green’s function associated with the linear reference homogeneous medium and the actual heterogeneous field [33]. All the local quantities can be written as the summation of a mean value

and a fluctuation indicated by a “~” symbol. Usually, the representative volume element of bulk microstructures (not on the surface) is modeled to be periodic and periodic boundary conditions are applied to control its deformation. In this case, the Fourier transform can be employed to efficiently solve the problem in Fourier space, where the convolution in the real space is reduced to simple product. An iterative scheme is needed to ensure that the solution converges to the micromechanical responses satisfying equilibrium and compatibility conditions.

For clarity, we will start with brief presentations of the solutions of pure elastic and pure visco-plastic problems. Then, the solution strategy of elasto-plastic problems will be introduced. For elasto-plastic problems, the strain rate is coupled with stress and stress rate leading to challenges in using the Green’s function method. To address this, we will introduce a solution strategy in which the elastic and plastic responses are computed simultaneously but separately.

2.1. Solution of Crystal Elastic Boundary Value Problems

In pure crystal elastic problems, the total strain rate $\dot{\boldsymbol{\epsilon}}$ is equal to the elastic strain rate $\dot{\boldsymbol{\epsilon}}^e$ and the stress rate is linearly related to the strain rate through the generalized Hooke’s law:¹

$$\dot{\boldsymbol{\sigma}}(\mathbf{x}) = \mathbf{C}^e(\mathbf{x}) : \dot{\boldsymbol{\epsilon}}^e(\mathbf{x}), \quad (1)$$

where $C_{ijkl}^e(\mathbf{x}) = R_{im}(\mathbf{x})R_{jn}(\mathbf{x})R_{ko}(\mathbf{x})R_{lp}(\mathbf{x})\check{C}_{mnop}^e$ is the local elastic stiffness tensor represented in the sample coordinate system that relates the crystal lattice frame via a rotation matrix $\mathbf{R}(\mathbf{x})$ determined by the orientation $\mathbf{r}(\mathbf{x})$ of the crystal at position \mathbf{x} . $\check{\mathbf{C}}^e$ is the elastic stiffness modulus in the lattice coordinate system.

For a microstructure subjected to periodic boundary conditions with an imposed average velocity gradient $\mathbf{L} = \nabla \mathbf{V}$, the local equilibrium equation, represented in terms of stress rate, needs to be satisfied at any point \mathbf{x} within the microstructure domain \mathcal{B} . The complete boundary value problem is defined as:

$$\begin{aligned} \nabla \cdot \dot{\boldsymbol{\sigma}}(\mathbf{x}) &= \nabla \cdot \tilde{\dot{\boldsymbol{\sigma}}}(\mathbf{x}) = 0 \quad \forall \mathbf{x} \in \mathcal{B}, \\ \tilde{\mathbf{v}}^e &\text{ is periodic,} \quad \dot{\boldsymbol{\sigma}} \cdot \mathbf{n} \text{ is antiperiodic on } \partial\mathcal{B}, \end{aligned} \quad (2)$$

¹We state the elastic problem in terms of stress and strain rates for exploring similarities with the formulation of the elasto-plastic problem in Section 2.2.

where $\tilde{\mathbf{v}}^e(\mathbf{x}) = \mathbf{v}^e(\mathbf{x}) - \mathbf{L} \cdot \mathbf{x}$ is the velocity fluctuation (deviation of the local velocity $\mathbf{v}^e(\mathbf{x})$ from the mean velocity \mathbf{V}) at \mathbf{x} induced by the microstructure heterogeneity. The superscript e indicates that the response stems from elastic deformation. Our goal is to compute the velocities and their gradients of all material points that satisfy the above governing equations and use them to evaluate the strain and stress responses over the microstructure domain. To this end, we can write the local stress $\boldsymbol{\sigma}(\mathbf{x})$ as the sum of two terms:

$$\dot{\boldsymbol{\sigma}}(\mathbf{x}) = \mathbf{C}^0 : \dot{\boldsymbol{\varepsilon}}^e(\mathbf{v}^e(\mathbf{x})) + \boldsymbol{\phi}^e(\mathbf{x}). \quad (3)$$

In Eq. (3), \mathbf{C}^0 is the stiffness modulus of a linear homogeneous reference medium, in which point \mathbf{x} is imbedded. In this elastic problem, \mathbf{C}^0 is selected as the averaged elastic modulus \mathbf{C}^e over the microstructure domain:

$$\mathbf{C}^0 = \mathbf{C}^{e0} = \langle \mathbf{C}^e \rangle_h = \frac{1}{V_B} \int_B \mathbf{C}^e(\mathbf{x}) d\mathbf{x}. \quad (4)$$

The second term, $\boldsymbol{\phi}^e(\mathbf{x})$, in Eq. (3) is the periodic polarization field defined as

$$\boldsymbol{\phi}^e(\mathbf{x}) = \dot{\boldsymbol{\sigma}}(\mathbf{x}) - \mathbf{C}^{e0} : \dot{\boldsymbol{\varepsilon}}^e(\mathbf{v}^e(\mathbf{x})) = \tilde{\dot{\boldsymbol{\sigma}}}(\mathbf{x}) - \mathbf{C}^{e0} : \tilde{\dot{\boldsymbol{\varepsilon}}}^e(\tilde{\mathbf{v}}^e(\mathbf{x})). \quad (5)$$

Substituting Eq. (3) into the equilibrium equation (Eq. (2)), we obtain

$$C_{ijkl}^{e0} \dot{\varepsilon}_{kl,j}^e + \phi_{ij,j}^e = 0 \quad \text{or} \quad C_{ijkl}^{e0} \tilde{\dot{\varepsilon}}_{kl,j}^e + \phi_{ij,j}^e = 0. \quad (6)$$

Representing the strain rate in terms of the velocity gradient $\dot{\varepsilon}_{ij}^e = \frac{1}{2} (v_{i,j}^e + v_{j,i}^e)$, we obtain:

$$C_{ijkl}^{e0} v_{k,lj}^e + \phi_{ij,j}^e = 0 \quad \text{or} \quad C_{ijkl}^{e0} \tilde{v}_{k,lj}^e + \phi_{ij,j}^e = 0. \quad (7)$$

The differential Eq. (7) can be solved by means of the Green's function method. Introducing the Green's function $\mathbf{G}^e(\mathbf{x}, \mathbf{x}')$, the solution $\tilde{v}_k^e(\mathbf{x})$ takes the form

$$\tilde{v}_k^e(\mathbf{x}) = - \int_B G_{km}^e(\mathbf{x} - \mathbf{x}') \phi_{mn,n}^e(\mathbf{x}') d\mathbf{x}'. \quad (8)$$

Substituting Eq. (8) into Eq. (7), leads to:

$$-C_{ijkl}^{e0} \int_B G_{km,lj}^e(\mathbf{x} - \mathbf{x}') \phi_{mn,n}^e(\mathbf{x}') d\mathbf{x}' + \int_B \delta_{im} \phi_{mj,j}^e(\mathbf{x}') \delta(\mathbf{x} - \mathbf{x}') d\mathbf{x}' = 0, \quad (9)$$

which can be rearranged as

$$\int_{\mathcal{B}} [-C_{ijkl}^{e0} G_{km,lj}^e(\mathbf{x} - \mathbf{x}') + \delta_{im} \delta(\mathbf{x} - \mathbf{x}')] \phi_{mn,n}^e(\mathbf{x}') d\mathbf{x}' = 0. \quad (10)$$

Taking $\phi_{mn,n}^e$ to be arbitrary, we arrive at the local equilibrium equation in the Green's function form:

$$-C_{ijkl}^{e0} G_{km,lj}^e(\mathbf{x} - \mathbf{x}') + \delta_{im} \delta(\mathbf{x} - \mathbf{x}') = 0. \quad (11)$$

This equation can be transformed to Fourier space where the convolutional solution in the real space (Eq. (8)) is represented by a simple product. The equilibrium equation in Fourier space is then:

$$\xi_l \xi_j C_{ijkl}^{e0} \hat{G}_{km}^e(\boldsymbol{\xi}) = -\delta_{im}, \quad (12)$$

where $\boldsymbol{\xi}$ is a point (frequency) in the Fourier space. Solving the linear system Eq. (12), we obtain the Green's function in Fourier space \hat{G}_{km}^e to be

$$\hat{\mathbf{G}}^e = \mathbf{A}^{e-1}, \quad A_{ik}^e = -\xi_l \xi_j C_{ijkl}^{e0}. \quad (13)$$

Defining

$$\hat{\Gamma}_{ijkl}^e = -\xi_l \xi_j \hat{G}_{ik}^e, \quad (14)$$

and integrating Eq. (8) by parts while assuming that the boundary terms vanish [32], we can compute the velocity fluctuation as:

$$\tilde{v}_k^e(\mathbf{x}) = \int_{\mathcal{B}} G_{km,n}^e(\mathbf{x} - \mathbf{x}') \phi_{mn}^e(\mathbf{x}') d\mathbf{x}'. \quad (15)$$

The velocity and its gradient fluctuations² in Fourier space are

$$\hat{\tilde{v}}_i^e(\boldsymbol{\xi}) = i \xi_j \hat{G}_{im}^e(\boldsymbol{\xi}) \hat{\phi}_{mj}^e(\boldsymbol{\xi}), \quad (16)$$

$$\hat{\tilde{v}}_{i,k}^e(\boldsymbol{\xi}) = \hat{\Gamma}_{ikmj}^e(\boldsymbol{\xi}) \hat{\phi}_{mj}^e(\boldsymbol{\xi}). \quad (17)$$

²Note that the fluctuations can also be total velocity and its gradient, depending on the assignment of the 0 frequency term.

After transforming them back to the real space (e.g. $\tilde{\mathbf{v}}^e(\mathbf{x}) = FFT^{-1}(\hat{\tilde{\mathbf{v}}}^e(\boldsymbol{\xi}))$), the strain rate and spin rate fluctuations can be evaluated, respectively, by

$$\begin{aligned}\tilde{\varepsilon}_{ij}^e(\mathbf{x}) &= \frac{1}{2}(\tilde{v}_{i,j}^e + \tilde{v}_{j,i}^e), \\ \tilde{\omega}_{ij}^e(\mathbf{x}) &= \frac{1}{2}(\tilde{v}_{i,j}^e - \tilde{v}_{j,i}^e).\end{aligned}\tag{18}$$

The stress rate can be updated according to the Hooke's Law (Eq.(1)). With the updated stress rate and strain rate, we can perform the next iteration until converged results are reached.

2.2. Solution of Crystal Visco-Plastic Boundary Value Problems

If the deformation is assumed to be pure visco-plastic (i.e. the elastic response is completely neglected, $\dot{\boldsymbol{\varepsilon}} = \dot{\boldsymbol{\varepsilon}}^p$). A nonlinear constitutive model is employed to link stress to strain rate in the form:

$$\dot{\boldsymbol{\varepsilon}}^p(\mathbf{x}) = \mathbf{M}^p(\boldsymbol{\sigma}(\mathbf{x})) : \boldsymbol{\sigma}(\mathbf{x}),\tag{19}$$

where $\mathbf{M}^p(\boldsymbol{\sigma}(\mathbf{x}))$ is a plastic compliance tensor that is nonlinearly dependent on stress $\boldsymbol{\sigma}(\mathbf{x})$.

The solution procedure of a visco-plastic problem is similar to that in Section 2.1 except that this time the equilibrium equation is written in terms of stress rather than stress rate:

$$\begin{aligned}\nabla \cdot \boldsymbol{\sigma}(\mathbf{x}) &= \nabla \cdot \tilde{\boldsymbol{\sigma}}(\mathbf{x}) = 0 \quad \forall \mathbf{x} \in \mathcal{B}, \\ \tilde{\mathbf{v}}^p &\text{ is periodic,} \quad \boldsymbol{\sigma} \cdot \mathbf{n} \text{ is antiperiodic on } \partial\mathcal{B},\end{aligned}\tag{20}$$

where the superscript p indicates plastic deformation induced response. Incompressibility of plastic deformation also needs to be satisfied. In [32], a Fourier transform-based algorithm was proposed where the incompressibility condition was satisfied by introducing explicitly the constraint $v_{k,k}^p = 0$. In the current work, the incompressibility condition is accounted for by computing the polarization $\boldsymbol{\phi}^p(\mathbf{x})$ with a strain rate updated iteratively as $\dot{\boldsymbol{\varepsilon}}^p \leftarrow \dot{\boldsymbol{\varepsilon}}^p - \frac{1}{3}tr(\dot{\boldsymbol{\varepsilon}}^p)$ as follows:

$$\boldsymbol{\phi}^p(\mathbf{x}) = \boldsymbol{\sigma}(\mathbf{x}) - \mathbf{C}^{p0} : \dot{\boldsymbol{\varepsilon}}^p(\mathbf{v}^p(\mathbf{x})) = \tilde{\boldsymbol{\sigma}}(\mathbf{x}) - \mathbf{C}^{p0} : \tilde{\dot{\boldsymbol{\varepsilon}}}^p(\tilde{\mathbf{v}}^p(\mathbf{x})),\tag{21}$$

where the stiffness modulus of the linear homogeneous reference medium is taken to be the averaged plastic modulus $\mathbf{C}^p = \mathbf{M}^{p-1}$ over the microstructure

domain:

$$\mathbf{C}^{p0} = \langle \mathbf{C}^p \rangle_h = \frac{1}{V_B} \int_B \mathbf{C}^p(\boldsymbol{\sigma}(\mathbf{x})) d\mathbf{x}. \quad (22)$$

The form of the plastic modulus \mathbf{C}^p or equivalently the plastic compliance \mathbf{M}^p is determined by the specific plastic constitutive model that is adopted. In Section 3, we will present two constitutive models to be used in the examples. The plastic problem can be solved following the steps from Eq. (6) to Eq. (18) simply by replacing the superscript e to p and using stress instead of stress rate.

2.3. Solution of Crystal Elasto-Plastic Boundary Value Problems

For elasto-plastic problems, the total strain rate $\dot{\boldsymbol{\epsilon}}$ is additively decomposed into an elastic term $\dot{\boldsymbol{\epsilon}}^e$ and a plastic part $\dot{\boldsymbol{\epsilon}}^p$ with $tr(\dot{\boldsymbol{\epsilon}}^p) = 0$:

$$\dot{\boldsymbol{\epsilon}}(\mathbf{x}) = \dot{\boldsymbol{\epsilon}}^e(\mathbf{x}) + \dot{\boldsymbol{\epsilon}}^p(\mathbf{x}). \quad (23)$$

Following the constitutive relations given above, both stress $\boldsymbol{\sigma}$ and stress rate $\dot{\boldsymbol{\sigma}}$ are entangled with strain rate:

$$\dot{\boldsymbol{\epsilon}}(\mathbf{x}) = \mathbf{M}^e(\mathbf{x}) : \dot{\boldsymbol{\sigma}}(\mathbf{x}) + \mathbf{M}^p(\boldsymbol{\sigma}(\mathbf{x})) : \boldsymbol{\sigma}(\mathbf{x}), \quad (24)$$

where $\mathbf{M}^e = \mathbf{C}^{e-1}$ is the elastic compliance tensor. The local mechanical response at time t depends on the entire loading history of the specimen. The current stress $\boldsymbol{\sigma}$ is computed by $\boldsymbol{\sigma} = \boldsymbol{\sigma}_n + \dot{\boldsymbol{\sigma}} dt$, where $\boldsymbol{\sigma}_n$ is the stress at the previous time step.

To follow a Green's function approach to the elasto-plastic boundary value problem, a proper modulus \mathbf{C}^0 , taking both elasticity and plasticity into account, needs to be designed for the homogeneous reference medium that can directly link either stress or stress rate to strain rate. However, to design such an effective modulus is not trivial. Therefore, we here propose a formulation that solves for the elastic and plastic velocity fluctuations separately using the fast Fourier transform-based algorithm thus avoiding the construction of the elasto-plastic modulus. The total velocity gradient at a single point is then computed by adding the two fluctuations to the mean value $\nabla \mathbf{V}$. After that, a nonlinear constitutive model is designed to update the stress and stress rate given the total strain rate. We will this approach as CEPFFT.

The key of the CEPFFT approach is that we solve simultaneously the two forms of the equilibrium equations defined in Eq. (2) and (20) for elastic and

plastic velocity (and their gradient) fluctuations. The total velocity gradient can then be obtained as

$$\nabla \mathbf{v}(\mathbf{x}) = \nabla \mathbf{V} + \nabla \tilde{\mathbf{v}}^e(\mathbf{x}) + \nabla \tilde{\mathbf{v}}^p(\mathbf{x}), \quad (25)$$

from which, the total strain rate $\dot{\boldsymbol{\epsilon}}$ can be calculated as the symmetric part of $\nabla \mathbf{v}$. However, the portion of elastic strain rate $\dot{\boldsymbol{\epsilon}}^e$ and plastic strain rate $\dot{\boldsymbol{\epsilon}}^p$ in $\dot{\boldsymbol{\epsilon}}$ is not known. As a result, the stress and stress rate corresponding to a given total strain rate cannot be directly computed.

An iterative scheme is designed to linearize the nonlinear relations among stress, stress rate, and strain rates, in order to provide a way of finding the elastic and plastic strain rates given the total strain rate. We first rewrite Eq. (23) as

$$\mathbf{F} = \dot{\boldsymbol{\epsilon}}^e(\mathbf{x}) + \dot{\boldsymbol{\epsilon}}^p(\mathbf{x}) - \dot{\boldsymbol{\epsilon}}(\mathbf{x}) = \mathbf{0}. \quad (26)$$

We aim at solving this equation for the elastic strain rate $\dot{\boldsymbol{\epsilon}}^e$ with known $\dot{\boldsymbol{\epsilon}}$ using the Newton-Raphson scheme. To this end, Eq. (26) can be linearized as follows:

$$\mathbf{F}^{(i+1)}(\dot{\boldsymbol{\epsilon}}^{e(i+1)}) = \mathbf{F}^{(i)}(\dot{\boldsymbol{\epsilon}}^{e(i)}) + \frac{d\mathbf{F}}{d\dot{\boldsymbol{\epsilon}}^e} (\dot{\boldsymbol{\epsilon}}^{e(i+1)} - \dot{\boldsymbol{\epsilon}}^{e(i)}). \quad (27)$$

According to the elastic and plastic constitutive models, as well as the stress incremental equation $\boldsymbol{\sigma} = \boldsymbol{\sigma}_n + \Delta t \dot{\boldsymbol{\sigma}}$, we can write the following relations:

$$\begin{aligned} \frac{d\dot{\boldsymbol{\epsilon}}^p}{d\boldsymbol{\sigma}} &= \mathbf{M}_t^p, \\ \frac{d\boldsymbol{\sigma}}{d\dot{\boldsymbol{\sigma}}} &= \frac{d(\boldsymbol{\sigma}_n + \Delta t \dot{\boldsymbol{\sigma}})}{d\dot{\boldsymbol{\sigma}}} = \Delta t \mathbf{II}, \\ \frac{d\dot{\boldsymbol{\sigma}}}{d\dot{\boldsymbol{\epsilon}}^e} &= \mathbf{C}^e, \end{aligned} \quad (28)$$

where \mathbf{II} is the fourth-order identity tensor and the tangent plastic compliance \mathbf{M}_t^p is specified by the particular plastic constitutive model used (see Section 3.1). Using these relations, we can simplify Eq. (27) as:

$$\begin{aligned} \mathbf{F}^{(i+1)}(\dot{\boldsymbol{\epsilon}}^{e(i+1)}) &= \mathbf{F}^{(i)}(\dot{\boldsymbol{\epsilon}}^{e(i)}) + \left(\frac{d\dot{\boldsymbol{\epsilon}}^e}{d\dot{\boldsymbol{\epsilon}}^e} + \frac{d\dot{\boldsymbol{\epsilon}}^p}{d\dot{\boldsymbol{\epsilon}}^e} \right) : (\dot{\boldsymbol{\epsilon}}^{e(i+1)} - \dot{\boldsymbol{\epsilon}}^{e(i)}) \\ &= \mathbf{F}^{(i)}(\dot{\boldsymbol{\epsilon}}^{e(i)}) + \left(\frac{d\dot{\boldsymbol{\epsilon}}^e}{d\dot{\boldsymbol{\epsilon}}^e} + \frac{d\dot{\boldsymbol{\epsilon}}^p}{d\dot{\boldsymbol{\epsilon}}^e} \frac{d\boldsymbol{\sigma}}{d\dot{\boldsymbol{\sigma}}} \frac{d\dot{\boldsymbol{\sigma}}}{d\dot{\boldsymbol{\epsilon}}^e} \right) : (\dot{\boldsymbol{\epsilon}}^{e(i+1)} - \dot{\boldsymbol{\epsilon}}^{e(i)}) \\ &= \mathbf{F}^{(i)}(\dot{\boldsymbol{\epsilon}}^{e(i)}) + (\mathbf{II} + \Delta t \mathbf{M}_t^p : \mathbf{C}^e) : (\dot{\boldsymbol{\epsilon}}^{e(i+1)} - \dot{\boldsymbol{\epsilon}}^{e(i)}). \end{aligned} \quad (29)$$

Setting $\mathbf{F}^{(i+1)} = \mathbf{0}$, the elastic strain rate at iteration $i + 1$ is computed by

$$\dot{\boldsymbol{\epsilon}}^{e(i+1)} = \dot{\boldsymbol{\epsilon}}^{e(i)} - (\mathbf{II} + \Delta t \mathbf{M}_t^p : \mathbf{C}^e)^{-1} : \mathbf{F}^{(i)}. \quad (30)$$

With the elastic strain rate $\dot{\boldsymbol{\epsilon}}^{e(i+1)}$ at the $(i+1)$ th iteration computed from the equation above, the stress rate $\dot{\boldsymbol{\sigma}}^{(i+1)}$ can be obtained using Eq. (1). Therefore, the stress is updated as $\boldsymbol{\sigma}^{(i+1)} = \boldsymbol{\sigma}_n + \dot{\boldsymbol{\sigma}}^{(i+1)}$, with which the plastic strain rate $\dot{\boldsymbol{\epsilon}}^{p(i+1)}$ can be computed using the plastic constitutive relation Eq. (19). The incompressibility is enforced by setting $\dot{\boldsymbol{\epsilon}}^{p(i+1)} \leftarrow \dot{\boldsymbol{\epsilon}}^{p(i+1)} - \frac{1}{3} \text{tr}(\dot{\boldsymbol{\epsilon}}^{p(i+1)}) \mathbf{I}$. Iteratively updating the above equations, the final elastic as well as the plastic strain rates can be computed until convergence is achieved (i.e. when \mathbf{F} in Eq. (26) approaches $\mathbf{0}$). The converged stress rate and stress can be subsequently computed according to the constitutive model. After that, we can construct the elastic and plastic polarization fields, respectively, following Eqs. (5) and (21). By transforming them to Fourier space, the fluctuations of velocity gradients induced by elastic and plastic deformation can be updated using Green's functions. Inversely transforming these fluctuations to real space, a new strain rate field as well as stress and stress rate can be obtained. The algorithm can then proceed to the next iteration. The overall CEPFFT algorithm is summarized next.

2.4. CEPFFT Algorithm

We adopt a basic fast Fourier transform-based algorithm for implementing the CEPFFT simulator. The algorithm was firstly proposed in [34, 35] to deal with elastic and elasto-plastic heterogeneous composites with moderate contrast. It was also adapted by Lebensohn [32] to solve elastic and visco-plastic polycrystalline problems. This method is based on the exact expression of Green's function for linear elastic, homogeneous reference material.

Algorithm:

1. At the first iteration, start with an initial guess of the total velocity gradient field at time step $n + 1$: ${}^0\nabla\mathbf{v}_{n+1}(\mathbf{x}) = \nabla\mathbf{v}_n(\mathbf{x}), \forall \mathbf{x} \in \mathcal{B}$, from which the local strain rate can be computed $\dot{\boldsymbol{\epsilon}}(\mathbf{x}) = \text{sym}(\nabla\mathbf{v}(\mathbf{x}))$. Then evaluate the elastic portion $\dot{\boldsymbol{\epsilon}}^e(\mathbf{x})$ and plastic portion $\dot{\boldsymbol{\epsilon}}^p(\mathbf{x})$ of the strain rate using the local constitutive relations. At the same time, compute the initial stress ${}^0\boldsymbol{\sigma}(\mathbf{x})$ and stress rate ${}^0\dot{\boldsymbol{\sigma}}(\mathbf{x})$.

2. Compute the elastic and plastic polarization fields, ${}^i\phi^e(\mathbf{x})$ and ${}^i\phi^p(\mathbf{x})$, respectively, for the i iteration given the stress, stress rate and strain rate fields:

$$\begin{aligned} {}^i\phi^e(\mathbf{x}) &= {}^i\dot{\boldsymbol{\sigma}}(\mathbf{x}) - \mathbf{C}^{e0} : {}^i\dot{\boldsymbol{\varepsilon}}^e(\mathbf{x}), \\ {}^i\phi^p(\mathbf{x}) &= {}^i\boldsymbol{\sigma}(\mathbf{x}) - \mathbf{C}^{p0} : {}^i\dot{\boldsymbol{\varepsilon}}^p(\mathbf{x}). \end{aligned} \quad (31)$$

3. Transform the polarizations to Fourier space via fast Fourier transform: ${}^i\hat{\phi}^e(\boldsymbol{\xi}) = FFT({}^i\phi^e(\mathbf{x}))$ and ${}^i\hat{\phi}^p(\boldsymbol{\xi}) = FFT({}^i\phi^p(\mathbf{x}))$.
4. Compute the velocity gradient fluctuation fields induced by elastic and plastic deformation, respectively, in the Fourier space for the $(i+1)$ -th iteration.

$$\begin{aligned} {}^{i+1}\nabla\hat{\mathbf{v}}^e(\boldsymbol{\xi}) &= \hat{\mathbf{\Gamma}}^e(\boldsymbol{\xi}) : {}^i\hat{\phi}^e(\boldsymbol{\xi}), \forall \boldsymbol{\xi} \neq \mathbf{0}; \quad \text{and} \quad {}^{i+1}\nabla\hat{\mathbf{v}}^e(\mathbf{0}) = \mathbf{0}, \\ {}^{i+1}\nabla\hat{\mathbf{v}}^p(\boldsymbol{\xi}) &= \hat{\mathbf{\Gamma}}^p(\boldsymbol{\xi}) : {}^i\hat{\phi}^p(\boldsymbol{\xi}), \forall \boldsymbol{\xi} \neq \mathbf{0}; \quad \text{and} \quad {}^{i+1}\nabla\hat{\mathbf{v}}^p(\mathbf{0}) = \mathbf{0}. \end{aligned} \quad (32)$$

5. Transform the current velocity gradient fluctuation fields back to the real space through inverse fast Fourier transform, i.e. ${}^{i+1}\nabla\tilde{\mathbf{v}}^e(\mathbf{x}) = FFT^{-1}({}^{i+1}\nabla\hat{\mathbf{v}}^e(\boldsymbol{\xi}))$ and ${}^{i+1}\nabla\tilde{\mathbf{v}}^p(\mathbf{x}) = FFT^{-1}({}^{i+1}\nabla\hat{\mathbf{v}}^p(\boldsymbol{\xi}))$.
6. Compute the total strain rate ${}^{i+1}\dot{\boldsymbol{\varepsilon}} = \dot{\mathbf{E}} + {}^{i+1}\tilde{\dot{\boldsymbol{\varepsilon}}}^e + {}^{i+1}\tilde{\dot{\boldsymbol{\varepsilon}}}^p$ and then the stress ${}^{i+1}\boldsymbol{\sigma}(\mathbf{x})$ and stress rate ${}^{i+1}\dot{\boldsymbol{\sigma}}(\mathbf{x})$ fields according to the constitutive model.
7. Check the error (equilibrium condition):

$$e = \frac{\langle \|\nabla \cdot {}^{i+1}\boldsymbol{\sigma}\|^2 \rangle^{1/2}}{\|{}^{i+1}\boldsymbol{\sigma}\|} = \frac{\langle \|\boldsymbol{\xi} \cdot {}^{i+1}\hat{\boldsymbol{\sigma}}\|^2 \rangle^{1/2}}{\|{}^{i+1}\hat{\boldsymbol{\sigma}}(\mathbf{0})\|}. \quad (33)$$

If e is smaller than a prescribed error tolerance, the iteration process stops. Otherwise, return to step (2) and proceed to the next iteration.

Upon convergence, the grain orientations and the positions of the pixel points are updated according to the spin and velocity gradient fields, respectively (see Section 4.3 for details).

Remark 1: The error of the equilibrium condition (Step (7)) is mostly determined by the resolution of the image (as will be shown later in the examples). For images with coarse resolution, the error may converge, with fluctuations, to a value larger than 0. This error is inherently associated

with the FFT-based methodology. Therefore, a practical way to check the convergence is to examine the relevant difference between the error at the current and last iterations:

$$\eta = \frac{|^{i+1}e - ^ie|}{^{i+1}e}. \quad (34)$$

Remark 2: It is clear that the computational cost of one iteration step of the algorithm discussed above is doubled that corresponding to either the pure elastic or visco-plastic algorithms. If a proper elasto-plastic modulus can be designed, the problem can be solved using only one set of equations, which may lead to higher computational efficiency. A feasible approach arises by representing the local stress $\boldsymbol{\sigma}(\mathbf{x})$ in terms of the total strain rate $\dot{\boldsymbol{\epsilon}}(\mathbf{v}(\mathbf{x}))$:

$$\boldsymbol{\sigma}(\mathbf{x}) = \mathbf{C}^0 : \dot{\boldsymbol{\epsilon}}(\mathbf{v}(\mathbf{x})) + \boldsymbol{\phi}(\mathbf{x}), \quad (35)$$

where $\mathbf{C}^0 = \langle \mathbf{C}^{ep} \rangle_h$ is computed as the volume average of an elasto-plastic modulus \mathbf{C}^{ep} derived as follows:

$$\mathbf{C}^{ep} = \frac{d\boldsymbol{\sigma}}{d\dot{\boldsymbol{\epsilon}}} = \frac{d\boldsymbol{\sigma}}{d\dot{\boldsymbol{\epsilon}}^e} \frac{d\dot{\boldsymbol{\epsilon}}^e}{d\dot{\boldsymbol{\epsilon}}} + \frac{d\boldsymbol{\sigma}}{d\dot{\boldsymbol{\epsilon}}^p} \frac{d\dot{\boldsymbol{\epsilon}}^p}{d\dot{\boldsymbol{\epsilon}}} = \Delta t \mathbf{C}^e + \mathbf{C}^p. \quad (36)$$

The plastic modulus \mathbf{C}^p is chosen to be the secant modulus that depends on the specifics of the constitutive model adopted. With the construction of the elasto-plastic modulus, the problem can be solved following the same procedure as for the visco-plastic problem. The convergence rate of this particular algorithm will be shown in Section 6 that is slower than the main algorithm presented earlier. A more sophisticated design of the elasto-plastic modulus is of great interest.

3. Constitutive Model

The fast Fourier transform based full field algorithm can be adapted to various materials assuming appropriate constitutive models are provided. In this section, we will describe two plastic constitutive models that are adopted in the numerical examples for single phase FCC crystal and IN100 superalloy. The plastic modulus that is needed in the CEPFFT method is derived. The fatigue indicator parameters that will be employed to measure the fatigue properties of Ni-based superalloys are defined in [44].

3.1. Plastic Constitutive Relations

Various plastic constitutive relations have been developed based on different flow rules and hardening laws. Usually, the nonlinear connection between plastic strain rate and Cauchy stress, $\dot{\boldsymbol{\epsilon}}^p(\boldsymbol{\sigma}(\mathbf{x}))$, is assumed, where the plastic strain rate $\dot{\boldsymbol{\epsilon}}^p$ is defined as the sum of the contributions of shear rates, $\dot{\gamma}^{(\alpha)}(\mathbf{x})$, on all active slip systems:

$$\dot{\boldsymbol{\epsilon}}^p(\mathbf{x}) = \sum_{\alpha}^{N_s} \mathbf{m}^{(\alpha)}(\mathbf{x}) \dot{\gamma}^{(\alpha)}(\mathbf{x}). \quad (37)$$

In the above equation, N_s is the number of active slip systems, and $\mathbf{m}^{(\alpha)}$ denotes the symmetric Schmid tensor of slip system α :

$$\mathbf{m}^{(\alpha)} = \text{sym}(\mathbf{S}^{(\alpha)}) = \frac{1}{2} (\mathbf{s}^{(\alpha)} \otimes \mathbf{n}^{(\alpha)} + \mathbf{n}^{(\alpha)} \otimes \mathbf{s}^{(\alpha)}), \quad (38)$$

where $\mathbf{s}^{(\alpha)}$ and $\mathbf{n}^{(\alpha)}$ are the slip direction and slip plane normal of the system α , respectively.

The shear rate $\dot{\gamma}^{(\alpha)}(\mathbf{x})$ is determined by the resolved shear stress $\tau^{(\alpha)} = \mathbf{S}^{(\alpha)} : \boldsymbol{\sigma} = \mathbf{m}^{(\alpha)} : \boldsymbol{\sigma}$ and slip resistance $\kappa^{(\alpha)}$ on slip system α through a specific flow rule. The difference between the various plastic constitutive models lies in the choice of the flow rule and hardening law that defines the evolution of the slip resistances.

3.1.1. A typical flow rule and hardening law for single phase crystalline materials

The first model we introduce here is a typical one for single phase polycrystals. Asaro and Needleman [6] proposed a widely used rate-dependent crystal plasticity flow rule for evaluating shearing rate, $\dot{\gamma}^{(\alpha)}$, on slip system α :

$$\dot{\gamma}^{(\alpha)} = \dot{\gamma}_0 \left| \frac{\tau^{(\alpha)}}{\kappa^{(\alpha)}} \right|^{(1/m)} \text{sign}(\tau^{(\alpha)}), \quad (39)$$

where $\dot{\gamma}_0$ is a reference rate of shearing and m characterizes the material rate sensitivity. $\kappa^{(\alpha)}$ is the slip resistance of system α . The slip resistance evolves following certain hardening law that is calibrated from experimental data to

describe the strain hardening effect. Currently, we adopt a Voce type model given in [40], where the hardening rate $\dot{\kappa}^{(\alpha)}$ is computed by

$$\dot{\kappa}^{(\alpha)} = \frac{d\bar{\kappa}^{(\alpha)}}{d\Gamma} \sum_{\beta} h^{\alpha\beta} \dot{\gamma}^{(\beta)}, \quad (40)$$

with the hardening function

$$\bar{\kappa}^{(\alpha)} = \kappa_0 + (\kappa_1 + \theta_1 \Gamma) \left[1 - \exp \left(-\frac{\theta_0 \Gamma}{\kappa_1} \right) \right], \quad (41)$$

where $h^{\alpha\beta}$ is a hardening matrix whose diagonal elements denote self-hardening and off-diagonal elements denote latent hardening. In the current work, we assume both of the two are identical and equal to 1. κ_0 , κ_1 , θ_0 , θ_1 are material dependent parameters. The cumulative shear Γ in a grain is defined as

$$\Gamma = \int_0^t \sum_{\alpha} \dot{\gamma}^{(\alpha)} \Delta t. \quad (42)$$

Following the above equations, we can derive an explicit form of the plastic constitutive law as

$$\dot{\boldsymbol{\epsilon}}^p(\mathbf{x}) = \mathbf{M}_s^p(\boldsymbol{\sigma}(\mathbf{x})) : \boldsymbol{\sigma}(\mathbf{x}), \quad (43)$$

where \mathbf{M}_s^p is called the secant plastic compliance having the form given below:

$$\mathbf{M}_s^p(\boldsymbol{\sigma}(\mathbf{x})) = \dot{\gamma}_0 \sum_{\alpha}^{N_s} \frac{\mathbf{m}^{(\alpha)}(\mathbf{x}) \otimes \mathbf{m}^{(\alpha)}(\mathbf{x})}{\kappa^{(\alpha)}(\mathbf{x})} \left| \frac{\mathbf{m}^{(\alpha)}(\mathbf{x}) : \boldsymbol{\sigma}(\mathbf{x})}{\kappa^{(\alpha)}(\mathbf{x})} \right|^{(1/m-1)}. \quad (44)$$

The corresponding tangent plastic compliance in Eq. (30) at this specific case is $\mathbf{M}_t^p = \frac{1}{m} \mathbf{M}_s^p$. The plastic modulus in Eq. (36) for the method highlighted in Remark 2 is $\mathbf{C}^p = \mathbf{M}_s^{p-1}$. Given a plastic strain rate, the corresponding stress needs to be computed following an iterative scheme (e.g. Newton-Raphson method) because of the nonlinear nature of the constitutive model.

3.1.2. A specific flow rule and hardening law for two-phase nickel-based superalloy IN100

In this work, we are also interested in the fatigue properties of IN100, a nickel-based superalloy, at high temperature (650°C). Since the microstructure of superalloys is complex, more sophisticated flow rule and hardening

laws are developed to describe the micromechanical behavior of two-phase microstructure. In this work, we employ the homogeneous constitutive model developed in [30]. The second phase (γ' precipitates) configuration is not explicitly modeled. Instead, the effects of the second phase are taken into account through particular parameters. Cube slip $\langle 110 \rangle \{100\}$ systems are activated in addition to octahedral slip $\langle 110 \rangle \{111\}$ systems to take cross slip mechanism at high temperatures into consideration. The rate dependent flow rule which estimates the shearing rate on each slip system includes a back force term χ for the modeling of the Baushinger effect arising principally from matrix dislocation interaction with γ' phase. The effect of volume and size of γ' precipitates on material strength is taken into account by constitutive parameters. The constitutive equations are summarized below and detailed in [30, 44, 45].

The flow rule of slip system α is

$$\begin{aligned} \dot{\gamma}^{(\alpha)} = & \left[\dot{\gamma}_1^{(\alpha)} \left\langle \frac{|\tau^{(\alpha)} - \chi_\lambda^{(\alpha)}| - \kappa_\lambda^{(\alpha)}}{D_\lambda^{(\alpha)}} \right\rangle^{n_1} \right. \\ & \left. + \dot{\gamma}_2^{(\alpha)} \left\langle \frac{|\tau^{(\alpha)} - \chi_\lambda^{(\alpha)}|}{D_\lambda^{(\alpha)}} \right\rangle^{n_2} \right] \text{sgn}(\tau^{(\alpha)} - \chi_\lambda^{(\alpha)}), \end{aligned} \quad (45)$$

where $\dot{\gamma}_1^{(\alpha)}$ and $\dot{\gamma}_2^{(\alpha)}$ are constants related to the initial shearing rate and $D_\lambda^{(\alpha)}$ is the drag stress assumed to be constant. $\lambda = \{\text{oct}, \text{cub}\}$ refers to the octahedral and cube slip systems, respectively. The function $\langle x \rangle$ returns x if $x > 0$ and returns 0, otherwise.

The evolution of the slip resistance $\kappa_\lambda^{(\alpha)}$ follows the Taylor strain hardening law determined by dislocation density $\rho_\lambda^{(\alpha)}$:

$$\kappa_\lambda^{(\alpha)} = \kappa_{0,\lambda}^{(\alpha)} + \alpha_t \mu_{mix} b \sqrt{\rho_\lambda^{(\alpha)}}, \quad (46)$$

where $\alpha_t = 0.0385$ and $\mu_{mix} = (f_{p1} + f_{p2} + f_{p3})\mu_{\gamma'} + f_m\mu_\gamma$. $\mu_{\gamma'}$ and μ_γ are shear moduli for γ' precipitates and γ matrix, respectively. The magnitude of Burgers vector is $b = (f_{p1} + f_{p2} + f_{p3})b_{\gamma'} + f_m b_\gamma$. f_{p1}, f_{p2}, f_{p3} are volume fractions of primary, secondary, and tertiary γ' precipitates, respectively, and $f_m = 1 - f_{p1} - f_{p2} - f_{p3}$ is the volume fraction of γ matrix phase. $f'_{p1} = \frac{f_{p1}}{f_{p1} + f_m}$, $f_{p2} = \frac{f_{p2}}{f_{p2} + f_m}$ and $f_{p3} = \frac{f_{p3}}{f_{p3} + f_m}$. For different slip systems, the initial slip resistance can be evaluated by

$$\kappa_{0,\text{oct}}^{(\alpha)} = \left[(\tau_{0,\text{oct}}^{(\alpha)})^{n_k} + \psi_{\text{oct}}^{n_k} \right]^{1/n_k} + (f_{p1} + f_{p2})\tau_{ns}^{(\alpha)},$$

$$\kappa_{0,cub}^{(\alpha)} = \left[(\tau_{0,cub}^{(\alpha)})^{n_k} + \psi_{cub}^{n_k} \right]^{1/n_k}, \quad (47)$$

where

$$\begin{aligned} \psi_\lambda &= c_{p1} \sqrt{w \frac{f'_{p1}}{d_1}} + c_{p2} \sqrt{w \frac{f'_{p2}}{d_2}} + c_{p3} \sqrt{w f'_{p3} d_3} + \frac{c_{gr}}{\sqrt{d_{gr}}}, \\ w &= \frac{\Gamma_{APB}}{\Gamma_{APB-ref}}, \end{aligned} \quad (48)$$

and

$$\tau_{ns}^{(\alpha)} = h_{pe} \tau_{pe}^{(\alpha)} + h_{cb} |\tau_{cb}^{(\alpha)}| + h_{se} \tau_{se}^{(\alpha)}, \quad (49)$$

in which Γ_{APB} is the anti-phase boundary energy density here taken be equal to $\Gamma_{APB-ref}$, $d_i, i = 1, 2, 3$ are the sizes of precipitates, and d_{gr} is the grain size. The non-Schmid stress $\tau_{ns}^{(\alpha)}$ is related to the resolved shear stresses on the primary $\tau_{pe}^{(\alpha)}$, cube $\tau_{cb}^{(\alpha)}$ and secondary $\tau_{se}^{(\alpha)}$ slip systems, respectively, by parameter h_{pe} , h_{cb} , and h_{se} . Currently, we assume this term to be 0.

The dislocation density evolution has the following form:

$$\begin{aligned} \dot{\rho}_\lambda^{(\alpha)} &= h_0 \left\{ Z_0 + k_{1,\lambda} \sqrt{\rho_\lambda^{(\alpha)}} - k_{2,\lambda} \rho_\lambda^{(\alpha)} \right\} |\dot{\gamma}^{(\alpha)}|, \\ Z_0 &= \frac{k_\delta}{b d_{\delta eff}}, \quad d_{\delta eff} \approx \left(\frac{2}{d_{2\delta}} \right)^{-1}. \end{aligned} \quad (50)$$

The evolution of the back stress $\chi_\lambda^{(\alpha)}$ is also dependent on dislocation density and shear rate:

$$\begin{aligned} \dot{\chi}_\lambda^{(\alpha)} &= C_\chi \left\{ \eta_\lambda \mu_{mix} b \sqrt{\rho_\lambda^{(\alpha)}} \operatorname{sgn}(\tau^{(\alpha)} - \chi_\lambda^{(\alpha)}) - \chi_\lambda^{(\alpha)} \right\} |\dot{\gamma}^{(\alpha)}|, \\ \eta_\lambda &= \frac{\eta_{0,\lambda} Z_0}{Z_0 + k_{1,\lambda} \sqrt{\rho_\lambda^{(\alpha)}}}, \end{aligned} \quad (51)$$

where $C_\chi = 123.93 - 433.98 f'_{p2} + 384.06 f_{p2}'^2$.

Parameters for superalloys at 650°C listed in [30] are adopted. For additional information about the constitutive model, the reader is referred to [44]. Given the stress, the plastic strain rate needs to be computed following the

nonlinear relationship and vice versa. Eq. (30) requires the evaluation of tangent plastic compliance. In the case of IN100 superalloy, the compliance can be derived as:

$$\begin{aligned}
\mathbf{M}_t^p(\mathbf{x}) &= \frac{d\dot{\boldsymbol{\varepsilon}}^p}{d\boldsymbol{\sigma}} = \sum_{\alpha}^{N_s} \left(\frac{d\dot{\boldsymbol{\varepsilon}}^p}{d\dot{\gamma}^{(\alpha)}} \frac{d\dot{\gamma}^{(\alpha)}}{d\tau^{(\alpha)}} \frac{d\tau^{(\alpha)}}{d\boldsymbol{\sigma}} \right) \\
&= \sum_{\alpha}^{N_s} \mathbf{m}^{(\alpha)}(\mathbf{x}) \otimes \mathbf{m}^{(\alpha)}(\mathbf{x}) \left[\dot{\gamma}_1 \frac{n_1}{D_{\lambda}^{(\alpha)}} \left\langle \frac{|\tau_{\lambda}^{(\alpha)} - \chi_{\lambda}^{(\alpha)}| - \kappa_{\lambda}^{(\alpha)}}{D_{\lambda}^{(\alpha)}} \right\rangle^{n_1-1} \right. \\
&\quad \left. + \dot{\gamma}_2 \frac{n_2}{D_{\lambda}^{(\alpha)}} \left\langle \frac{|\tau_{\lambda}^{(\alpha)} - \chi_{\lambda}^{(\alpha)}|}{D_{\lambda}^{(\alpha)}} \right\rangle^{n_2-1} \right]. \tag{52}
\end{aligned}$$

The secant plastic modulus required by Eqs. (21) and (36) is taken to be $\mathbf{C}^p = \mathbf{M}_s^{p-1}$ with

$$\begin{aligned}
\mathbf{M}_s^p(\mathbf{x}) &= \sum_{\alpha}^{N_s} \mathbf{m}^{(\alpha)}(\mathbf{x}) \otimes \mathbf{m}^{(\alpha)}(\mathbf{x}) \left[\dot{\gamma}_1 \frac{1}{D_{\lambda}^{(\alpha)}} \left\langle \frac{|\tau_{\lambda}^{(\alpha)} - \chi_{\lambda}^{(\alpha)}| - \kappa_{\lambda}^{(\alpha)}}{D_{\lambda}^{(\alpha)}} \right\rangle^{n_1-1} \right. \\
&\quad \left. + \dot{\gamma}_2 \frac{1}{D_{\lambda}^{(\alpha)}} \left\langle \frac{|\tau_{\lambda}^{(\alpha)} - \chi_{\lambda}^{(\alpha)}|}{D_{\lambda}^{(\alpha)}} \right\rangle^{n_2-1} \right]. \tag{53}
\end{aligned}$$

With these relations, the algorithm proposed in Section 2 can be applied to IN100 superalloy.

4. Microstructure Model

The solution strategy of computing the deformation of polycrystalline microstructures under periodic boundary conditions was discussed in Section 2. The main procedure is: (1) compute polarization field; (2) transform the polarization field to Fourier space using fast Fourier transform; (3) update velocity gradient in the Fourier space and transform it back to the real space; (4) update real-space fields (e.g. strain rate, spin rate, stress rate, etc.) accordingly. An iterative scheme is adopted to obtain convergence. In this section, we would introduce the digital microstructure model that is used as the input to FFT-based simulations. The update strategy of the microstructure and crystal orientation during deformation is also described.

4.1. Discretization

The input to the FFT-based (including pure elastic, pure visco-plastic, and elasto-plastic) simulators is pixelized images with orientation parameters associated with each pixel (or voxel for 3D). The pixels or voxels are the discretization of the input image, which essentially requires no effort.

To implement the FFT-based algorithm and solve the underlying boundary value problem, the microstructure is discretized by a regular grid consisting of $N_1 \times N_2$ pixels (2D problem) or $N_1 \times N_2 \times N_3$ voxels (3D problem). Denote L_i to be the period (edge length) of the microstructure in the i th direction ($i = 1, 2$ for 2D and $i = 1, 2, 3$ for 3D). The coordinates of the point, which is pixel in 2D and voxel in 3D, in the i th direction is therefore:

$$x_i = 0, \frac{L_i}{N_i}, 2\frac{L_i}{N_i}, \dots, (N_i - 1)\frac{L_i}{N_i}. \quad (54)$$

In Fig. 1, examples of 2D and 3D grids of polycrystalline microstructures are shown in comparison with their image views. Different colors in the microstructure represent grains with distinct orientations. The grain structures are generated following a Voronoi tessellation scheme, where the positions of centroids are adjusted to minimize the interaction forces [46] (see Section 4.2).

The regular discretization grid of the microstructure determines a regular reciprocal grid in the Fourier space, which makes the fast Fourier transform convenient. The i -th direction coordinates of the points in the reciprocal grid, namely frequencies, are

$$\xi_i = \left(-\frac{N_i}{2} + 1\right) \frac{1}{L_i}, \left(-\frac{N_i}{2} + 2\right) \frac{1}{L_i}, \dots, -\frac{1}{L_i}, 0, \frac{1}{L_i}, \dots, \left(\frac{N_i}{2} - 1\right) \frac{1}{L_i}, \left(\frac{N_i}{2}\right) \frac{1}{L_i}, \quad (55)$$

where $i = 1, 2$ for 2D and $i = 1, 2, 3$ for 3D. In the current work, the number of points in each dimension is selected to be a power of 2 in order to facilitate the fast Fourier transform that is conducted using the FFTW libraries [47].

4.2. Microstructure Generation

The microstructure image can be generated by several experimental or numerical ways, e.g. electron backscattered diffraction (EBSD), phase field method, Monte Carlo grain growth, or Voronoi tessellation. In the current

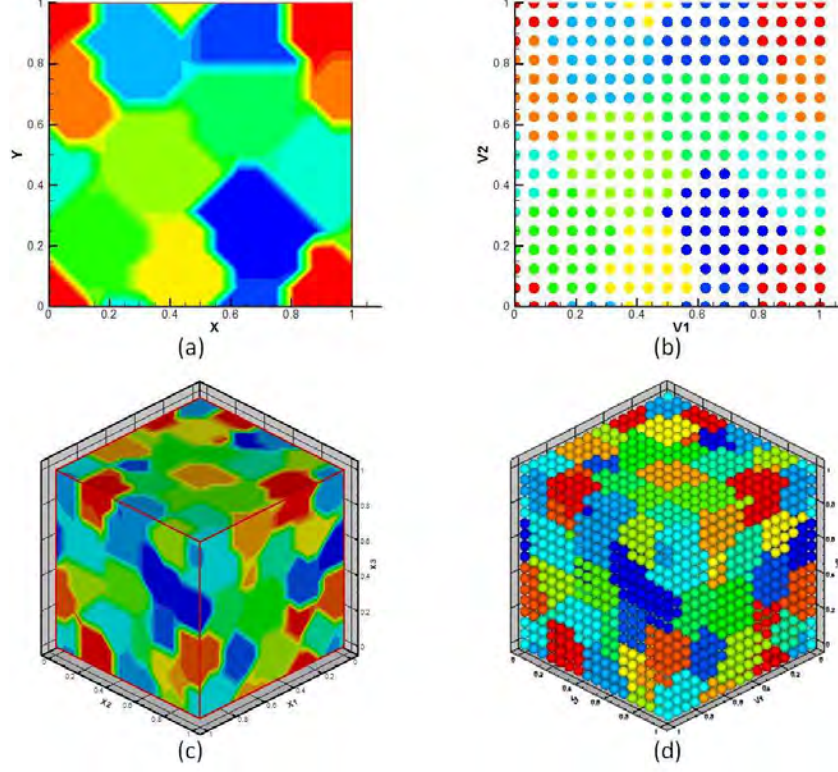


Figure 1: (a) The image representation of a 2D polycrystalline microstructure containing 10 grains. (b) The pixel grid of the 10-grain 2D microstructure. The microstructure is discretized by 16×16 pixels. (c) The image representation of a 3D polycrystalline microstructure containing 64 grains. (b) The voxel grid of the 64-grain 3D microstructure. The microstructure is discretized by $16 \times 16 \times 16$ voxels.

work, we adopt the Voronoi tessellation scheme in combination with a “relaxation” strategy to generate polycrystalline microstructures with approximately controlled grain sizes. The algorithm is summarized as follows:

- Given a set of target sizes of the microstructure constituent grains, we first randomly place Voronoi cell centroids within the microstructure domain. The number of centroid points, N_p , is decided by $N_p = V/\mu_d$, where V is the microstructure volume (for 3D) or area (for 2D), and μ_d is the mean volume or area of grains.
- A force function $\mathbf{F}(i, j)$ is defined for the adjustment of grain centroid

locations:

$$\mathbf{F}(i, j) = \mathbf{n}(j, i) * \langle r(i) + r(j) - \text{dist}(i, j) \rangle, \quad (56)$$

where $\mathbf{F}(i, j)$ is the force exerted by point j on point i in the direction $\mathbf{n}(j, i)$, which is along the line starting from j and pointing to i . $r(i)$ is the radius (assuming spherical (for 3D) or circular (for 2D) grains) of grain i . $\text{dist}(i, j)$ is the distance between point i and point j , which can be periodic if the microstructure is periodic. Function $\langle x \rangle = x$, if $x > 0$, and $\langle x \rangle = 0$, otherwise.

- Relaxation step: move points according to the velocity function defined as

$$\mathbf{v}(i) = \mathbf{F}(i)/V(i), \quad (57)$$

where $\mathbf{F}(i)$ is the net force of point i : $\mathbf{F}(i) = \sum_j \mathbf{F}(i, j)$ and $V(i)$ is the volume or area of the corresponding grain. The location of centroid i is updated to $\mathbf{P}_{n+1}(i) = \mathbf{P}_n(i) + \mathbf{v}(i)\Delta t$, where Δt adaptively changes for the convenience of convergence.

- After all centroid locations are stable (force balance is reached), a Voronoi tessellation is computed using them. The polycrystalline microstructure is therefore constructed.

A schematic description of relaxation of the Voronoi cell centroids is depicted in Fig. 2.

4.3. Grid and Texture Update

The grid after deformation may become irregular as material points move according to local velocities. The exact new position of material point \mathbf{X} is

$$\mathbf{x}(\mathbf{X}) = \mathbf{X} + (\mathbf{L} + \nabla \tilde{\mathbf{v}}(\mathbf{X})) \mathbf{X} \Delta t, \quad (58)$$

where $\mathbf{L} = \nabla \mathbf{V}$ is the homogeneous (average) velocity gradient of the microstructure and $\tilde{v}_{i,j}(\mathbf{x})$ is the velocity gradient fluctuation at point \mathbf{x} .

To model the deformation of the microstructure, an irregular material grid is expected. However, this irregular grid in the real space results in difficulties on conducting Fourier transform in the next time step in a time-dependent simulation, because that fast Fourier transform requires a regular grid. To

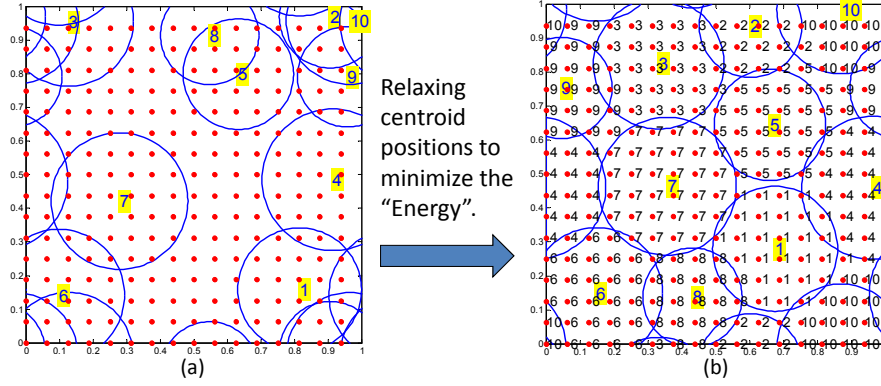


Figure 2: (a) The initial randomly placed Voronoi cell centroids with corresponding circular grain envelopes. (b) The relaxed centroids which are used for Voronoi tessellation. The microstructure is assumed to be periodic. Numbers in figures are grain IDs.

resolve this complexity, a strategy of using two grids, a regular computation grid and an irregular material configuration grid, proposed in [43] based on the Particle-In-Cell (PIC) method [48, 49] is introduced. The computation grid is used for applying the fast Fourier transform method to evaluate the strain related fields. It is a regular grid but not necessary rectangular as required by Fourier transform. The material grid, on the other hand, is attached to material particles, on which constitutive relations are carried out.

Each grid carries its own set of unknowns. Information needs to be transferred back and forth between the two grids during computation. At the beginning of each time step, the initial guess of local stress and polarization are computed on the material grid given the initial strain rate. The polarization field is transferred to the computation grid, on which fast Fourier transform is performed. The updated velocity gradient is then transferred back to the material grid so that the stress related fields can be updated using the constitutive model. At the end of the time step, the computation and material grids are deformed. The material particles move according to local velocity (Eq. (58)) and the regular computation grid evolves with the average velocity gradient:

$$\mathbf{x}(\mathbf{X}) = (\mathbf{I} + \mathbf{L}\Delta t) \mathbf{X}. \quad (59)$$

A schematic showing the operation of the multi-grid strategy is depicted in Fig. 3.

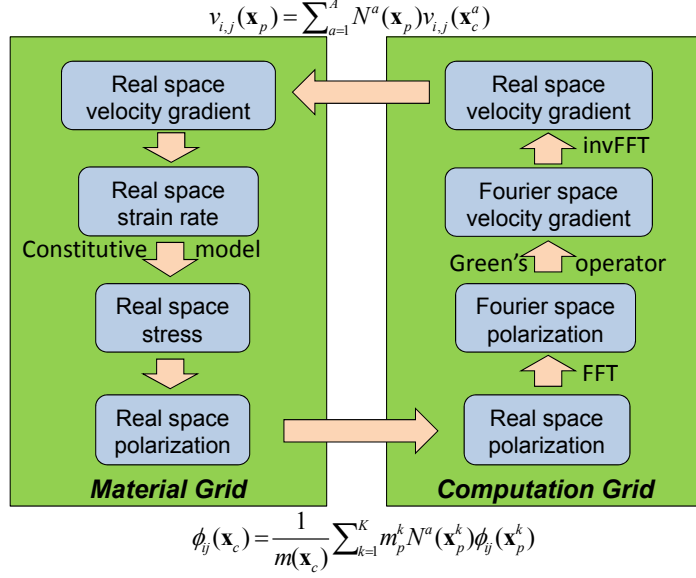


Figure 3: A schematic description of the multi-grid CEPFFT strategy. The constitutive model is applied only on the material grid, whereas fast Fourier transform operates on the computation grid.

The information transfer from regular computation grid to material points is performed through an interpolation operation. A family of shape functions $N^a(\mathbf{x})$, $a = 1, \dots, A$ are introduced. Since the regular computation grid forms quadrilateral (in 2D) or brick (in 3D) elements, a natural choice of N^a are the classical finite element shape functions. Given nodal values $f_c(\mathbf{x}_c^a)$ of a function $f(\mathbf{x})$ on the computation grid (denoted by subscript c), the interpolated value at any material point \mathbf{x}_p in the microstructure (denoted by subscript p) is given as

$$f_p(\mathbf{x}_p) = \sum_a^A N^a(\mathbf{x}_p) f_c(\mathbf{x}_c^a). \quad (60)$$

The interpolation is local since finite element shape functions are adopted. Only nodes belonging to the element that contains particle \mathbf{x}_p are involved.

The inverse transfer from the material grid to the computation grid is performed using the same interpolation functions [43]. We assume all material particles have the same mass m_p . The mass of a computational node is

defined as

$$m_c(\mathbf{x}_c) = \sum_k^K m_p^k N^a(\mathbf{x}_p^k). \quad (61)$$

The sum is over all material particles that are contained in the elements that share a common computation node \mathbf{x}_c . N^a is the corresponding shape function that connects particle \mathbf{x}_p^k to node \mathbf{x}_c . The function value f_c of f at any computation node \mathbf{x}_c is therefore:

$$f_c(\mathbf{x}_c) = \frac{1}{m_c(\mathbf{x}_c)} \sum_k^K m_p^k N^a(\mathbf{x}_p^k) f_p(\mathbf{x}_p^k). \quad (62)$$

A 2D illustration of initial and deformed computation and material grids is shown in Fig. 4, where big red spots represent material particles and small black spots are the nodes of the computation grid. The deformed computation grid remains regular so that fast Fourier transform can be conducted, while material particles move heterogeneously. In most PIC studies, the material grid is finer than the computational one. In the current work, however, we employ the same resolution of the two grids.

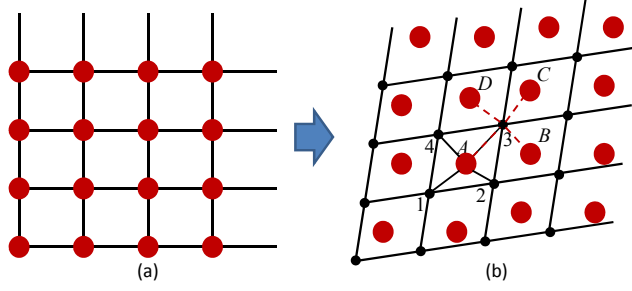


Figure 4: (a) Initial computation and material grids. (2) Deformed computation and material grids. The red dots denote material particles and the black dots denote nodes of the computation grid. The solid black lines show the connection between one material particle (A) and computation nodes and the red dashed lines are the connections between one computation node (3) and surrounding material particles.

This multi-grid strategy requires extra computation time. In the literature, one regular grid is used and the material grid is assumed to coincide with the computation grid at all times [38, 40]. In the current work, we will

conduct simulations primarily using this single-grid simplification. Comparison with the multi-grid results are demonstrated. It will be shown that for the examples considered, the mechanical responses computed from the multi- or single-grid approaches do not vary significantly although the deformed microstructures have distinct geometry.

The orientations of crystals also evolve with deformation. Upon convergence, the local crystallographic lattice rotations can be updated by the spin rate calculated by

$$\dot{\boldsymbol{\omega}}(\mathbf{x}) = \dot{\boldsymbol{\Omega}} + \tilde{\dot{\boldsymbol{\omega}}}(\mathbf{x}) - \dot{\boldsymbol{\omega}}^{slip}(\mathbf{x}), \quad (63)$$

where $\dot{\boldsymbol{\Omega}} = \text{antisym}(\nabla \mathbf{V})$ is the average spin rate over the microstructure domain. $\tilde{\dot{\boldsymbol{\omega}}}(\mathbf{x}) = \tilde{\dot{\boldsymbol{\omega}}}^e(\mathbf{x}) + \tilde{\dot{\boldsymbol{\omega}}}^p(\mathbf{x})$ is the spin rate fluctuation induced by elastic and plastic rotation. The last term that is subtracted is the rotation rate due to plastic shear (slip) that does not distort the crystal lattice. It is calculated by

$$\dot{\boldsymbol{\omega}}^{slip}(\mathbf{x}) = \sum_{\alpha}^{N_s} \boldsymbol{\beta}^{(\alpha)} \cdot \dot{\gamma}^{(\alpha)}, \quad (64)$$

where $\boldsymbol{\beta}^{(\alpha)}$ is the anti-symmetric Schmid tensor ($\boldsymbol{\beta}^{(\alpha)} = \text{antisym}(\mathbf{S}^{(\alpha)}) = \frac{1}{2}(\mathbf{s}^{(\alpha)} \otimes \mathbf{n}^{(\alpha)} - \mathbf{n}^{(\alpha)} \otimes \mathbf{s}^{(\alpha)})$, and $\mathbf{s}^{(\alpha)}$, $\mathbf{n}^{(\alpha)}$ are slip direction and normal to the slip plane of the α -th slip system, respectively).

5. Crystal Plasticity Finite Element Method

We will compare the CEPFFT results with conventional full-field crystal plasticity finite element method adopting a total Lagrangian scheme [27] developed in our previous work [29]. The reference configuration of each time step is the original undeformed microstructure. The total deformation gradient \mathbf{F} is multiplicatively decomposed into an elastic part \mathbf{F}^e and a plastic part \mathbf{F}^p .

$$\mathbf{F} = \mathbf{F}^e \mathbf{F}^p, \quad (65)$$

where plastic deformation is volume conserved: $|\mathbf{F}^p| = 1$.

The velocity gradient of plastic deformation \mathbf{L}^p is determined by slip rates on all slip systems:

$$\mathbf{L}^p = \dot{\mathbf{F}}^p \mathbf{F}^{p-1} = \sum_{\alpha} \dot{\gamma}^{(\alpha)} \mathbf{s}^{(\alpha)} \otimes \mathbf{n}^{(\alpha)}. \quad (66)$$

The plastic strain rate and spin rate are calculated by $\dot{\boldsymbol{\epsilon}}^p = \text{sym}(\mathbf{L}^p)$ and $\dot{\boldsymbol{\omega}}^p = \text{antisym}(\mathbf{L}^p)$, respectively. The same flow rule (e.g. Eq. (39)) and hardening law (e.g. Eq. (40)) as in the CEPFFT model are employed for estimating shearing rates $\dot{\gamma}^{(\alpha)}$.

The orientation computed at Gauss points is updated using the elastic deformation gradient as:

$$\begin{aligned}\mathbf{s}^{(\alpha)} &= \mathbf{R}^e \mathbf{s}_0^{(\alpha)}, \\ \mathbf{n}^{(\alpha)} &= \mathbf{R}^{e-T} \mathbf{n}_0^{(\alpha)},\end{aligned}\tag{67}$$

where \mathbf{R}^e is the rotation part of \mathbf{F}^e , and $\mathbf{s}_0^{(\alpha)}$ and $\mathbf{n}_0^{(\alpha)}$ are slip direction and plane normal of the α -th slip system of the undeformed grain.

6. Numerical examples

In this section, numerical examples conducted using the fast Fourier transform based approach are presented. Comparison between different formulations (e.g. visco-plasticity vs. elasto-plasticity) and between different methods (finite element method vs. fast Fourier transform based methods) are conducted to validate the current developments. In addition, the basic FFT methodology presented earlier is compared with the augmented Lagrangian approach introduced in [40, 33]. Mechanical response and fatigue properties measured by strain based fatigue indicator parameters [50] of IN100 microstructures are studied using the novel CEPFFT method. The computational efficiency of CEPFFT and crystal plasticity finite element method are presented to show the merit of the CEPFFT method. The use of the multi-grid strategy is also discussed.

6.1. Basic formulation versus the augmented Lagrangian formulation

We will start with a benchmark plane strain example of 3D polycrystalline microstructure simulated using the crystal visco-plasticity fast Fourier transform method (elastic response is neglected). The crystal visco-plastic constitutive model is implemented in the basic framework highlighted earlier in this paper as well as using the so called augmented Lagrangian formulation [40, 33]. The single-grid strategy is adopted so that deformation fluctuations are neglected.

FCC aluminum is considered. A cubic polycrystalline microstructure composed of 64 grains is generated using the Voronoi tessellation scheme in

an 1mm^3 domain. The microstructure is discretized by $16 \times 16 \times 16$ equally spaced voxels. The macroscale velocity gradient is

$$\mathbf{L} = \nabla \mathbf{V} = \begin{bmatrix} 0.0 & 0.0 & 0.0 \\ 0.0 & 1.0 & 0.0 \\ 0.0 & 0.0 & -1.0 \end{bmatrix} \times 10^{-3} (s^{-1}). \quad (68)$$

The rate-dependent flow rule (Eq. (39)) is used with $\dot{\gamma}_0 = 1s^{-1}$ and $m = 0.1$. The hardening model given in Eq. (40) is adopted to update slip resistances. The parameters in the hardening law are selected according to [40]: $\kappa_0 = 47.0\text{MPa}$, $\kappa_1 = 86.0\text{MPa}$, $\theta_0 = 550.0\text{MPa}$, and $\theta_1 = 16.0\text{MPa}$. An arbitrary random texture is assigned to the microstructure. The initial microstructure configuration and pole figures showing the random orientation distribution are shown in Fig. 5.

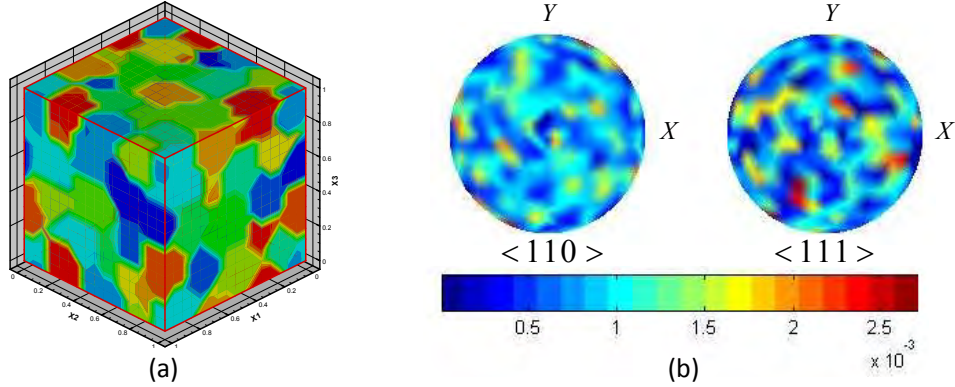


Figure 5: (a) The image representation of a 3D polycrystalline microstructure containing 64 grains. (b) Pole figures of the microstructure with randomly assigned orientations.

This example is used to validate the implementation of the general FFT framework by providing a comparison with the alternative augmented Lagrangian implementation. After the thickness of the microstructure reduces by 50%, the deformed microstructure and its stress and strain fields are plotted in Fig. 6. For both implementations, the stress distribution over the microstructure is consistent with the grain geometry. The local mechanical responses of the two simulations are very close. Both intergranular and intragranular heterogeneities of the stress and strain rate fields are captured.

The volume-averaged effective stress-strain responses of the entire microstructure computed by the two different algorithms are shown in Fig. 7(a).

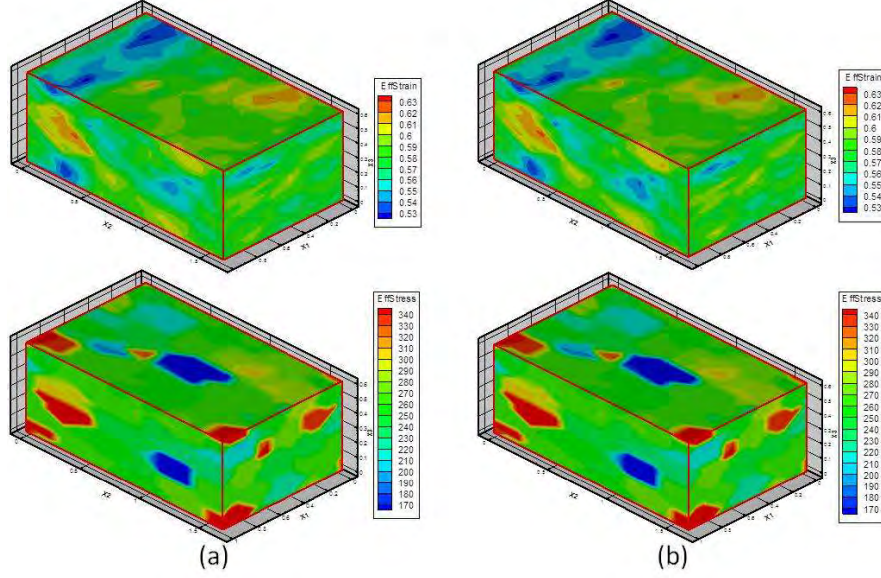


Figure 6: Contour plots of plane strain deformed microstructures evaluated by different algorithms. The top layer is the equivalent (plastic) strain field, and the bottom layer is the equivalent stress field. (a) Crystal visco-plasticity fast Fourier transform approach implemented in the basic formulation (b) Crystal visco-plasticity fast Fourier transform approach implemented in the augmented Lagrangian formulation.

The two curves overlap. Pole figures showing the orientation distribution of deformed microstructure are depicted in Fig. 7(b), from which we observe the typical plane strain deformation texture pattern for both cases.

From the above comparison of the local and effective mechanical responses, we conclude that consistent results are obtained from the two algorithms. An error analysis study for this problem also has revealed that the equilibrium error has similar convergence for both approaches. This fact proves that there is no need for an augmented Lagrangian implementation of the FFT algorithm and that the basic formulation has sufficiently accurate performance for solving polycrystal plasticity problems [51].

It is also worth mentioning that the equilibrium error is mostly determined by the resolution of the microstructure. For high resolution, the equilibrium condition is fulfilled with smaller error (see Fig. 8). When the number of pixels per side is doubled, the equilibrium error is approximately halved.

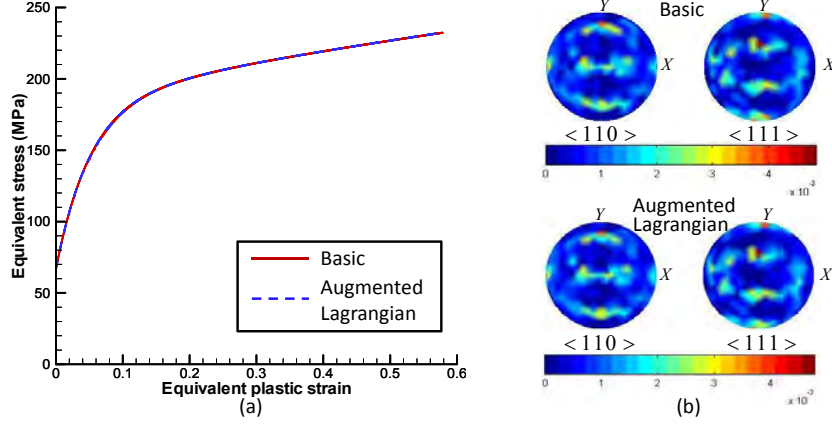


Figure 7: (a) The macroscopic effective stress-strain responses computed by the basic and augmented Lagrangian crystal visco-plasticity FFT algorithms. (b) Pole figures of the deformed microstructure texture.

6.2. Crystal elasto-plastic FFT simulations for polycrystalline microstructures

We consider here the same example as in Section 6.1 using the CEPFFT method. Both the microstructure configuration and material parameters are identical to the previous example. The elastic constants in the elasto-plastic model are chosen to be $C_{11} = 110 \times 10^3 \text{MPa}$, $C_{12} = 59 \times 10^3 \text{MPa}$, $C_{44} = 26 \times 10^3 \text{MPa}$. The CEPFFT results are compared with the pure visco-plastic computation as well as the results obtained from the crystal plasticity finite element method. Both multi-grid and single-grid strategies are also adopted and compared.

In the finite element simulation, homogeneous boundary condition is applied to the microstructure to drive its deformation while the boundary conditions of FFT-based simulations are periodic. The homogeneous boundary condition enforces all boundary nodes to have the same deformation/velocity gradient (e.g. Eq. (68) for the current plane strain problem), but heterogeneous nodal response inside the microstructure is allowed. This homogeneous boundary condition will result in different local mechanical responses on the microstructure from those obtained using the periodic boundary condition, but the macroscopic effective response should be comparable. The FEM simulation is conducted using our in-house solver extended based on [29].

We first adopt the main CEPFFT proposed in Section 2.4 with single-grid strategy to perform simulations. The total strain, plastic strain, and stress

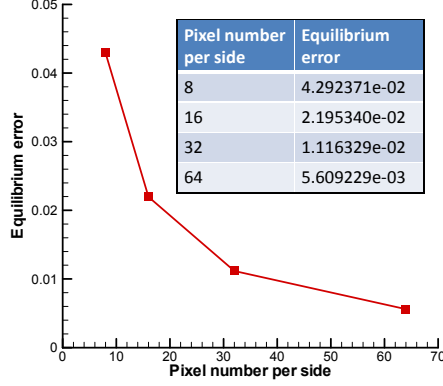


Figure 8: Equilibrium error as a function of resolution (number of pixels per side). The equilibrium error is evaluated when the convergence error reaches below 10^{-7} .

fields of the deformed microstructure after 50% thickness reduction computed by different models are plotted in Fig. 9. It is seen that CEPFFT gives very consistent prediction to both strain and stress fields with the pure viscoplastic results obtained in Section 6.1. The magnitude of the plastic strain field prediction by CEPFFT is slightly smaller than the one predicted by visco-plastic approach. On the other hand, the fields predicted by the FFT-based simulations show differences (especially for strain fields) from those based on crystal plasticity finite element simulations. The major causes of the differences between the FFT-based methods and the FEM approach include: (1) the different boundary conditions (periodic by the FFT-based methods and homogeneous by FEM), (2) the grain in FFT-based simulation is assigned to the digital model in the unit of “point” while it is assigned to the finite element model in the unit of “element” (each element contains 8 points), (3) the fast Fourier transform results are computed directly on the voxel points while the finite element results are computed on integration points and extrapolated to nodes using a least squares method, and (4) algorithmic differences. However, we notice that the stress fields exhibit similar patterns. This is because the mean strains predicted by the two methods are about the same and much larger in value than the strain fluctuations. One thing is also worth mentioning is that the spatial variation of strain fields predicted by crystal plasticity finite element method is actually on the same level with CEPFFT. In the contour plots, the values shown in the finite element results is adjusted to be smaller than in CEPFFT in order to show the strain variation on boundary nodes, where homogeneous deformation is applied.

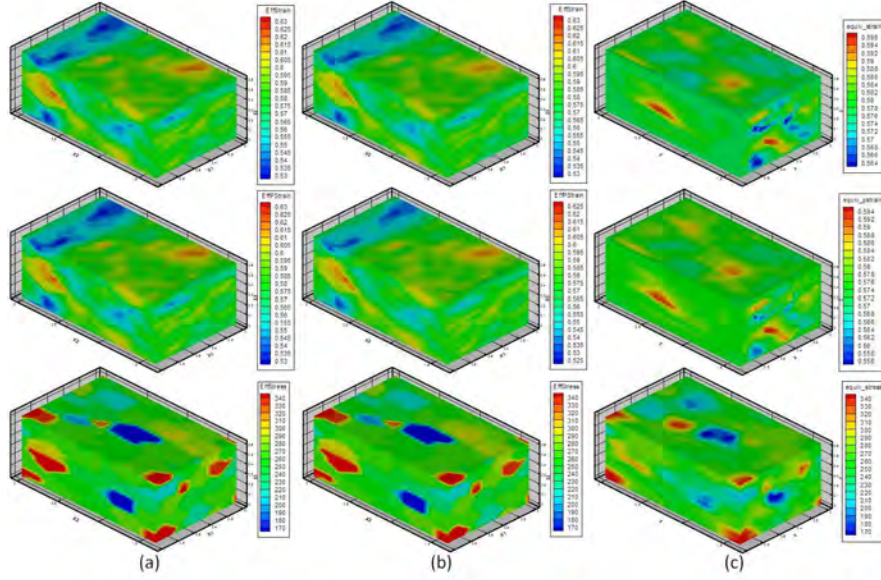


Figure 9: Contour plots of plane strain deformed microstructures evaluated by different methods. The first row is the equivalent total strain field, the second row is the equivalent plastic strain field, and the bottom row is the equivalent stress field. (a) Crystal viscoplasticity fast Fourier transform method. The total strain and plastic strain are identical here since the elastic response is ignored in this model. (b) Crystal elasto-plasticity fast Fourier transform method (CEPFFT) (c) Crystal plasticity finite element method.

The macroscopic effective stress-strain responses of the entire microstructure are compared in Fig. 10. The elastic response is successfully captured by the CEPFFT model and is comparable to the finite element prediction. It is observed that CEPFFT gives close prediction to the macroscopic response with finite element approach even though the boundary conditions for the two approaches are different.

The textures predicted by the three models are plotted using pole figures in Fig. 11. It is observed that all the three sets of pole figures predicted are very similar. The typical plane strain pattern is obtained.

To check the convergence of the results with respect to increasing resolution, we performed the same simulation on the same microstructure but discretized by $32 \times 32 \times 32$ voxels using CEPFFT. The local and effective mechanical responses are compared in Figs. 12 and 13, respectively. It is observed that the two sets of results are consistent. Plotted in the two figures are also the predictions using the modified CEPFFT approach introduced in

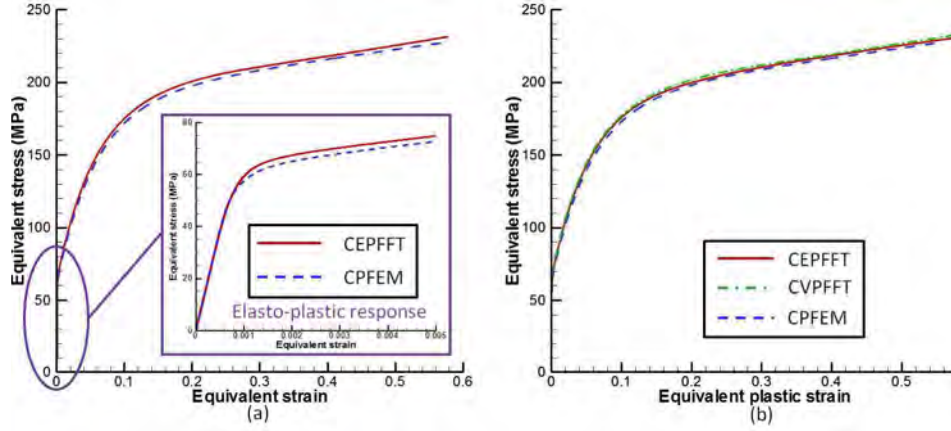


Figure 10: The macroscopic effective stress-strain responses of plane strain deformed microstructures predicted by different models. (a) Effective stress-total strain responses by CEPFFT and crystal plasticity FEM; (b) The effective stress-plastic strain responses by the three methods. Note that here CVPFFT denotes crystal visco-plasticity fast Fourier method, and CPFEM refers to crystal plasticity finite element method.

Remark 2, where stress is linked to total strain rate through an elasto-plastic modulus. We observe that the results from this modified implementation are close to the main formulation of this paper (that computes elastic and plastic fluctuations separately), although with milder spatial variation, implying its good performance for this problem.

We also studied the equilibrium error of the main CEPFFT approach for microstructures with different resolution. The improvement of error with refining the image is seen from Fig. 14(a), which is similar to the visco-plasticity case. The convergence of the CEPFFT model as a function of iteration number is shown in Fig. 14(b). We observe a fast convergence rate for all tests.

In order to check the effect of heterogeneous deformation on mechanical responses, we next repeat the above simulations with the multi-grid strategy. implemented with the CEPFFT. The deformed material grid obtained by the multi-grid strategy and the homogeneous approximation are plotted in Fig. 15. Contour plots of local mechanical responses are shown in Fig. 16. Comparing with the single-grid results, we find that the predicted mechanical responses do not vary much, although the deformed microstructures becomes irregular. The effective stress-strain curve and grain orientation distribution predicted by the multi-grid strategy are almost identical with the correspond-

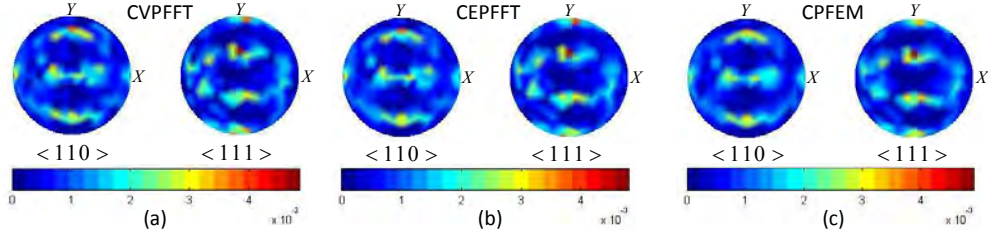


Figure 11: Crystallographic textures, represented in pole figures, of plane strain deformed microstructures predicted by three models. (a) Crystal visco-plasticity fast Fourier transform method (CVPFFT) (b) Crystal elasto-plasticity fast Fourier transform method (CEPFFT) (c) Crystal plasticity finite element method (CPFEM).

ing results obtained with the single-grid prediction and are not repeated here.

We next examine an example of volume-conserved compression using three different models. The same polycrystalline microstructure containing 64 grains and material parameters are used, while the imposed velocity gradient becomes

$$\mathbf{L} = \nabla \mathbf{V} = \begin{bmatrix} 0.5 & 0.0 & 0.0 \\ 0.0 & 0.5 & 0.0 \\ 0.0 & 0.0 & -1.0 \end{bmatrix} \times 10^{-3} (s^{-1}). \quad (69)$$

The single-grid strategy along with the main CEPFFT formulation is firstly adopted. After the compression in z direction reaches 50%, the total strain, plastic strain, and stress fields are plotted in Fig. 17. The local mechanical fields obtained from visco-plasticity and elasto-plasticity approaches agree very well. We also observe that the finite element stress and strain field results show very similar pattern with the FFT-based results despite the different kinematic conditions imposed on the FEM and FFT methodologies.

The macroscopic effective stress-strain responses of the entire microstructure are compared in Fig. 18. The elastic response is also successfully captured by the CEPFFT model and is comparable with the finite element prediction.

The crystallographic textures described by pole figures are also captured (Fig. 19). We can see once more that the different models give very close prediction on the texture evolution of the volume-conserved compression.

To check the convergence of the results with respect to increasing resolution for volume-conserved compression deformation, we also performed the

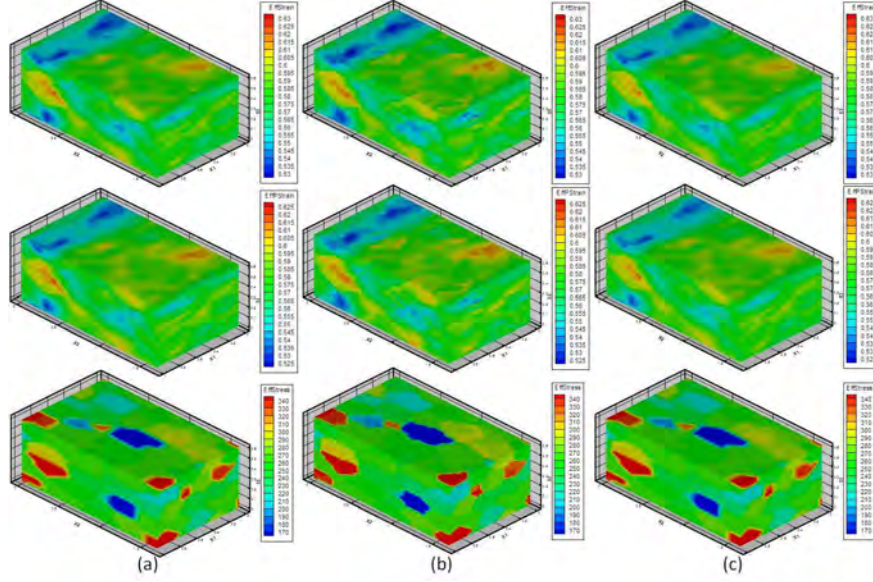


Figure 12: Contour plots of plane strain deformed microstructures with different resolution and methods. The first row is the equivalent total strain field, the second row is the equivalent plastic strain field, and the bottom row is the equivalent stress field. (a) The main CEPFFT method using $16 \times 16 \times 16$ -voxel microstructure. (b) The main CEPFFT method using $32 \times 32 \times 32$ -voxel microstructure. (c) The modified CEPFFT (Remark 2) using $16 \times 16 \times 16$ -voxel microstructure.

same simulation on the same microstructure but discretized by $32 \times 32 \times 32$ voxels. The local and effective mechanical responses are compared in Figs. 20 and 21, respectively. The results computed using the modified CEPFFT formulation discussed in Remark 2 are also demonstrated. Both the local and effective responses are close for the two implementations of the CEPFFT method.

Comparing the multi-grid with the single-grid results, we note that the irregular deformation is captured (Fig. 22), while the mechanical responses do not exhibit obvious change (Fig. 23). Almost identical effective stress-strain response and texture evolution with the single-grid prediction are observed and as such these results are not shown here.

6.3. Investigation of fatigue indicator parameters of IN100

In this subsection, we adapt the CEPFFT method to study fatigue properties of Ni-based superalloys using the flow rule and hardening law for the

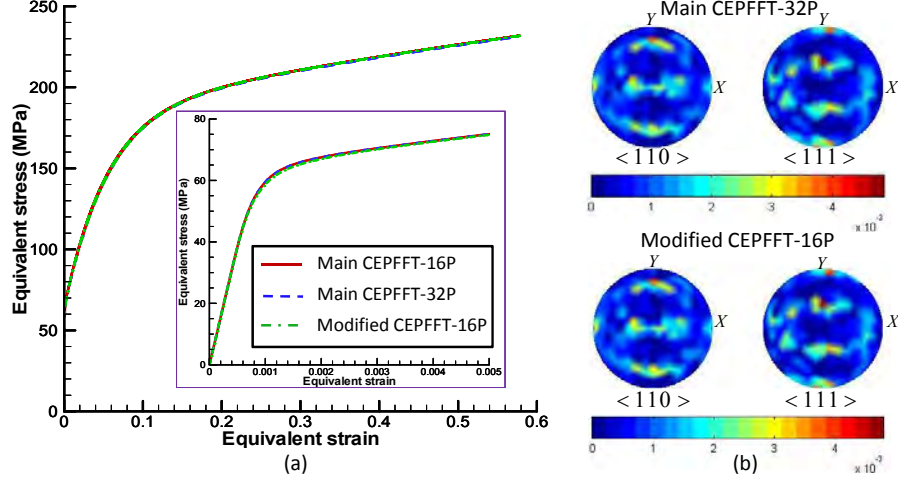


Figure 13: (a) The macroscopic effective stress-total strain responses by $16 \times 16 \times 16$ microstructure and $32 \times 32 \times 32$ microstructure obtained using different formulations. (b) Crystallographic textures represented in pole figures. Main CEPFFT refers to the main crystal elasto-plasticity FFT method and Modified CEPFFT refers to the crystal elasto-plasticity implementation using a homogeneous elasto-plastic medium approach (Remark 2).

IN100 model introduced in Section 3.1.2. The same microstructure configuration as in the previous examples is used and the initial texture is random. The same parameters of the constitutive equations as listed in [30] are used. The volume fractions and sizes of γ' precipitates are given by $f_{p1} = 0$, $f_{p2} = 0.42$, $d_2 = 108nm$, $f_{p3} = 0.11$, $d_3 = 7nm$. The microstructure is subjected to a 3-loop cyclic loading (tension and compression along the z -direction). The stress-strain response in the z -direction during the 3 loading loops is plotted in Fig. 24 with comparison to an FEM simulation that adopts the same constitutive model. The CEPFFT models implemented in both the main formulation and the modified formulation (in Remark 2) are tested. The single-grid update strategy is adopted. The microstructure input to the CEPFFT simulation is discretized by $16 \times 16 \times 16$ voxels to be consistent with the finite element input ($16 \times 16 \times 16$ cubic elements). Homogeneous boundary condition is applied to the finite element microstructure. The CEPFFT simulations give similar prediction to the stress-strain “loop” with the finite element model. Note that the loop predicted by the main CEPFFT algorithm is wider than the loops obtained from the FEM or the modified CEPFFT algorithm.

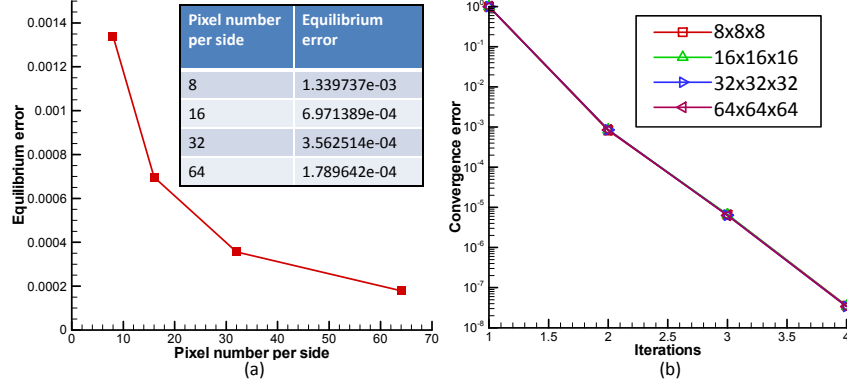


Figure 14: (a) Equilibrium error as a function of resolution (number of pixels per side). The equilibrium error is evaluated using the basic formulation when the convergence error reaches below 10^{-7} . (b) Convergence error versus number of iterations.

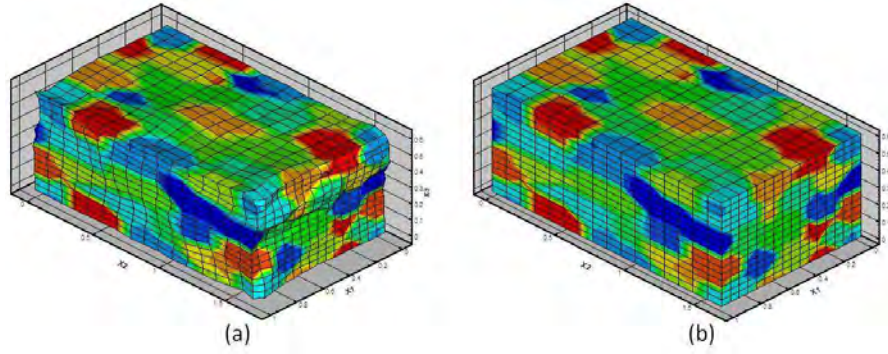


Figure 15: (a) Deformed microstructure predicted by multi-grid CEPFFT. (b) Deformed microstructure predicted by single-grid CEPFFT.

We next compute strain based fatigue indicator parameters (FIPs) related to small crack formation and early growth [50]. The three fatigue indicator parameters of interest are the cumulative plastic strain per cycle (P_{cyc}), which correlates to the crack incubation life; the Fatemi-Socie parameter (P_{FS}), which relates to the small crack growth; and the maximum range of cyclic plastic shear strain parameter (P_{mps}). The definitions of these fatigue indicator parameters can be found in [44]. Contour plots of fatigue indicator parameters over the microstructure are plotted in Fig. 25. All fatigue indicator parameters are computed for the last (3rd) loading loop. We observe that the fatigue indicator parameters contour plots demonstrate similar patterns in CEPFFT and crystal plasticity finite element simulations. The results

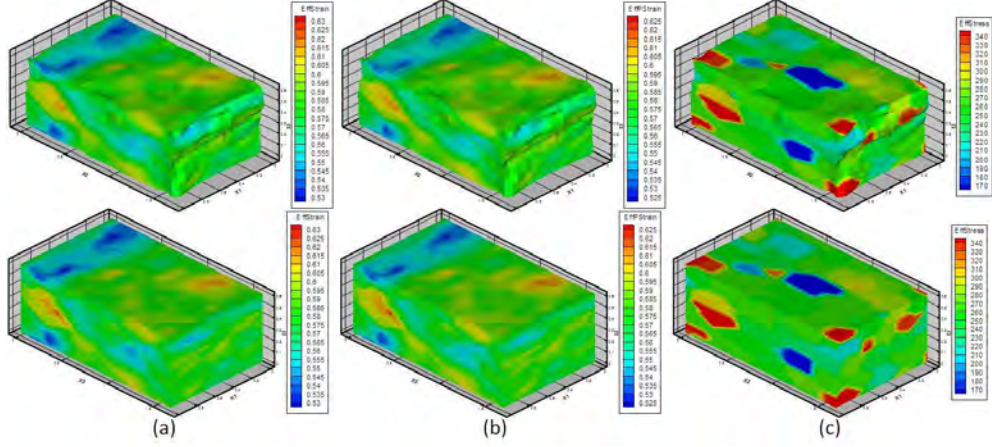


Figure 16: Contour plots of plane strain deformed microstructures computed using different strategies. The first row shows results obtained from the multi-grid CEPFFT, and the bottom row shows results obtained from the single-grid CEPFFT. (a) Equivalent total strain (b) Equivalent plastic strain (c) Equivalent stress.

predicted by the main CEPFFT approach show more heterogeneity and are closer to finite element results than the modified FFT model (Remark 2).

The convergence of the CEPFFT simulation with respect to resolution and the multi-grid effect are also tested for this fatigue problem. The fatigue indicator parameters are plotted in Fig. 26. It is observed that the deformation heterogeneity does not affect significantly the fatigue indicator parameters fields and the distortion of the microstructure is small since the total strain is small for this problem. The finer microstructure ($32 \times 32 \times 32$ voxels) gives consistent prediction to local fatigue indicator parameters with the coarse grid prediction, while larger heterogeneity is captured.

Grain level fatigue indicator parameters, namely the maximum and average fatigue indicator parameters of voxels within individual grains [44] are also extracted. Their distributions are shown in Fig. 27. The distributions computed using the main CEPFFT based on the $16 \times 16 \times 16$ -voxel microstructure are shown in (a). The ones computed using the main CEPFFT on the $32 \times 32 \times 32$ -voxel microstructure are plotted in (b). The results of the modified implementation of CEPFFT (Remark 2) are depicted in (c), and the crystal plasticity finite element results are given in (d). These results are obtained using the single-grid strategy. In the figure, the FIP with “max” prefix means the maximum value of the FIP of voxels within an individual

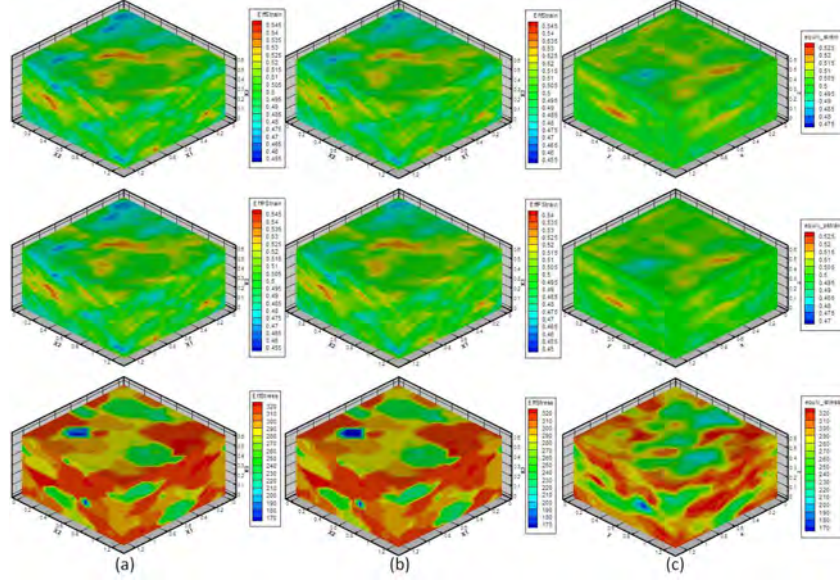


Figure 17: Contour plots of compressed microstructures evaluated by different methods. The first row is equivalent total strain field, the second row is equivalent plastic strain field, and the bottom row is equivalent stress field. (a) Crystal visco-plasticity fast Fourier transform method (CVPFFT). The total strain and plastic strain are identical here since the elastic response is ignored in this model. (b) Crystal elasto-plasticity fast Fourier transform method (CEPFFT). (c) Crystal plasticity finite element method (CPFEM).

grain. The one with “ave” prefix indicates that it is the average FIP over voxels within an individual grain. The distributions are normalized by the maximum value of each FIP over all grains of the microstructure. It is seen that the distributions of grain level fatigue indicator parameters predicted by the main CEPFFT on the finer microstructure are closer to the finite element results. The ones predicted by the main CEPFFT on coarse microstructure are also close to the fine microstructure estimations. On the other hand, the maximum and average fatigue indicator parameters distributions predicted by the modified CEPFFT are not very distinguishable, implying that the intragranular heterogeneity of fatigue indicator parameters predicted by the modified CEPFFT formulation is weak. This is consistent with the contour plots of the FIP fields. A more sophisticated elasto-plastic modulus may resolve this problem.

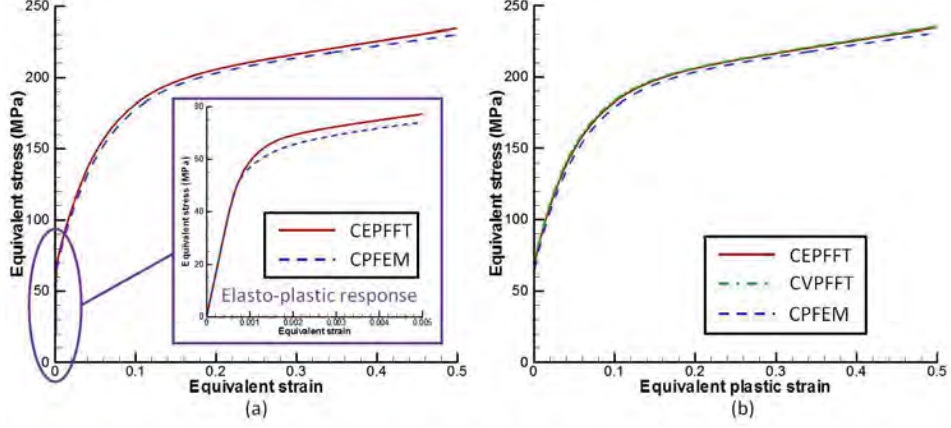


Figure 18: The macroscopic effective stress-strain responses of compressed microstructures predicted by different models. (a) Effective stress-total strain responses by CEPFFT and crystal plasticity finite element method (CPFEM); (b) Effective stress-plastic strain responses by all three methods. CVPFFT refers to crystal visco-plasticity fast Fourier method.

6.4. Computation Efficiency

The computational efficiency of CEPFFT method is important since our goal is to develop a high efficient full-field simulator that can be adopted in stochastic simulations as the deterministic solver to further study the probabilistic nature of material properties. As mentioned before, with the employment of fast Fourier transform to solve for local mechanical responses, the cumbersome matrix inversion in finite element simulation is circumvented, which leads to great improvement of the computation speed. The computation times of microstructures subjected to plane strain deformation to 0.02 strain are shown in Fig. 28(a) and tabulated in Table 1. All tests were run on the Teragrid TACC Lonestar Linux Cluster. Each computation node contains two Xeon Intel Hexa-Core 64-bit Westmere processors, the core frequency of which is $3.33GHz$. Single-grid morphology evolution strategy and main formulation are adopted by all CEPFFT tests. We first ran examples on one single processor, respectively. The CEPFFT simulation of a microstructure discretized by 16^3 voxels only takes less than 3 minutes, while the finite element simulation of a microstructure containing 16^3 elements takes 13 hours. With an increased resolution of 32^3 voxels, the computation time of CEPFFT increases to about 22 minutes, which is still significantly smaller than the finite element simulation. In order to further reduce the computation time,

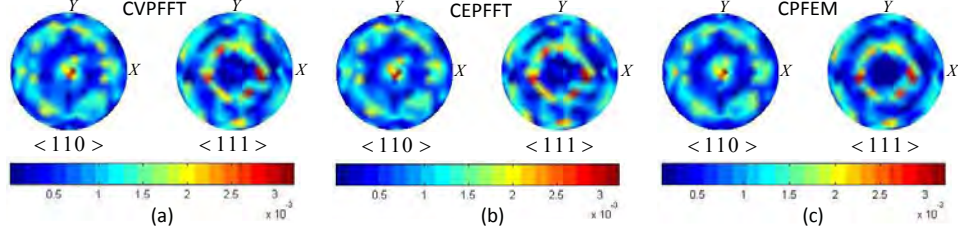


Figure 19: Crystallographic textures, represented in pole figures, of compressed microstructures predicted by three models. (a) Crystal visco-plasticity fast Fourier transform method (CVPFFT). (b) Crystal elasto-plasticity fast Fourier transform method (CEPFFT). (c) Crystal plasticity finite element method (CPFEM).

Table 1: Computation times for microstructures under plane strain and cyclic deformations simulated using different methods. CPFEM refers to crystal plasticity finite element method.

	1-processor, CEPFFT, 16 ³ -voxel	60-processor, CEPFFT, 16 ³ -voxel	1-processor, CEPFFT, 32 ³ -voxel	240-processor, CEPFFT, 32 ³ -voxel	1-processor, CPFEM, 16 ³ -element	240-processor, CPFEM, 16 ³ -element
Plane strain	164s	5s	1309s	17s	46389s	560s
Cyclic loading	554s	16s	4385s	57s	46873s	522s

we also parallelized our code. The 16³-voxel CEPFFT simulation only takes 5 seconds to finish if run on 60 processors. The 32³-voxel simulation running on 240 processors takes 17 seconds to finish. On the other hand, the finite element simulation of 16³-element microstructure takes about 10 minutes to complete when 240 processors are used.

Besides plane strain deformation, we also tested the computational efficiency of the microstructure fatigue problem. The computation times of one complete loading loop are captured and plotted in Fig. 28(b). We observe, again, that the CEPFFT simulation is much faster than the crystal plasticity finite element method. Note that the time increment required by the finite element simulation is smaller than that required by the fast Fourier transform simulation in order to reach convergence. However, even if the two approaches use the same time increment, the FFT computation is still much faster than the FEM simulation for the microstructure resolution.

With the adoption of fast Fourier transform for solving the polycrystalline microstructure boundary value problem, the most time consuming operation

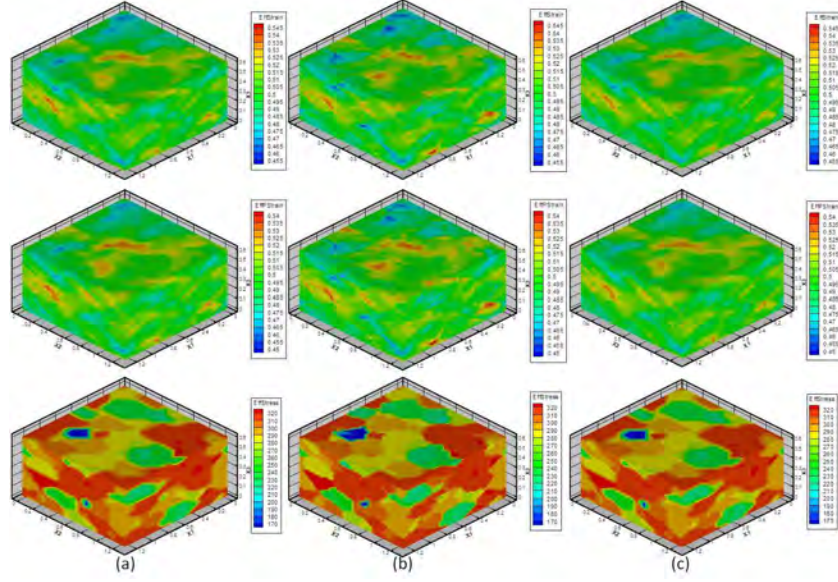


Figure 20: Contour plots of compressed microstructures with different resolution and formulation. The first row is the equivalent total strain field, the second row is the equivalent plastic strain field, and the bottom row is the equivalent stress field. (a) The main CEPFFT using $16 \times 16 \times 16$ -voxel microstructure. (b) The main CEPFFT method using $32 \times 32 \times 32$ -voxel microstructure (c) The CEPFFT method implemented using a homogeneous elasto-plastic medium approach (Remark 2) using $16 \times 16 \times 16$ -voxel microstructure.

in the FFT-based simulation is then the nonlinear constitutive calculations defined by the crystal plasticity theory. Another branch of research using Fourier methods in computational crystal plasticity has been conducted by Kalidindi and coworkers, who have introduced Fourier expansion to establish hypersurfaces of constitutive equations so that the iterative computation in updating nonlinear local properties can be approximated using spectral interpolation [52, 53, 54, 55]. Different from our strategy of solving the overall microstructure governing equations using Fourier transform, they replace nonlinear local constitutive equations by Fourier expansion after calibrating coefficients of the Fourier series using a given database. The computation efficiency of a crystal plasticity problem may be further improved by coupling their spectral method with the present crystal plasticity fast Fourier transform framework.

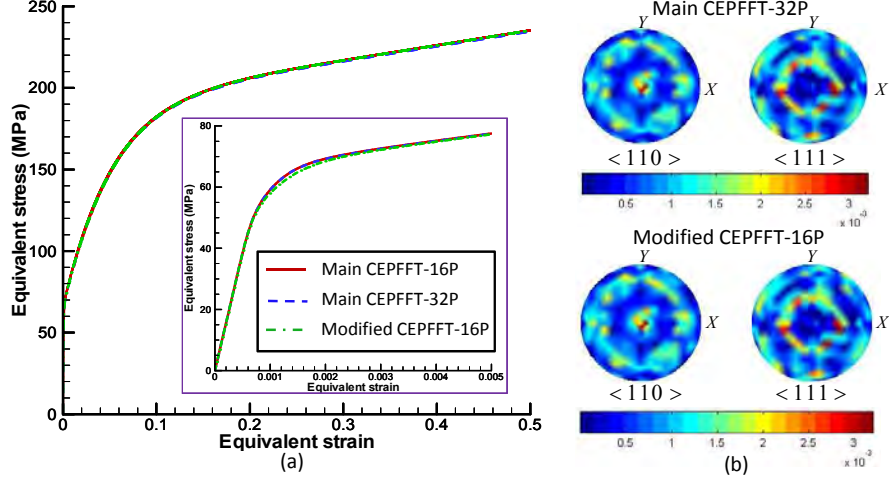


Figure 21: (a) The macroscopic effective stress-total strain responses by $16 \times 16 \times 16$ microstructure and $32 \times 32 \times 32$ microstructure obtained using different formulations. (b) Crystallographic textures represented in pole figures. Main CEPFFT refers to the main crystal elasto-plasticity FFT method and Modified CEPFFT refers to the crystal elasto-plasticity implementation using a homogeneous elasto-plastic medium approach (Remark 2).

7. Conclusions

In this work, we developed an efficient FFT full field model to investigate elasto-plastic properties of polycrystalline materials by interrogating image-based realistic microstructures. The elastic and plastic responses were computed separately. An integrated formulation was also proposed using a particular choice for the elasto-plastic moduli. Predictive capability and computational efficiency of the newly developed CEPFFT method were presented using numerical examples in comparison with visco-plasticity approach and crystal plasticity finite element simulations. Error tests were conducted to show the comparable performance of the basic and augmented Lagrangian algorithms. The multi-grid strategy was implemented to allow comparison with the single-grid simplification. The self-consistence (convergence with refining discretization) of the CEPFFT method was shown through simulations with increasing resolution of the microstructure. Fatigue properties of Ni-based superalloy microstructures described by fatigue indicator parameters were studied using the CEPFFT method. The main discoveries of this work are as follows:

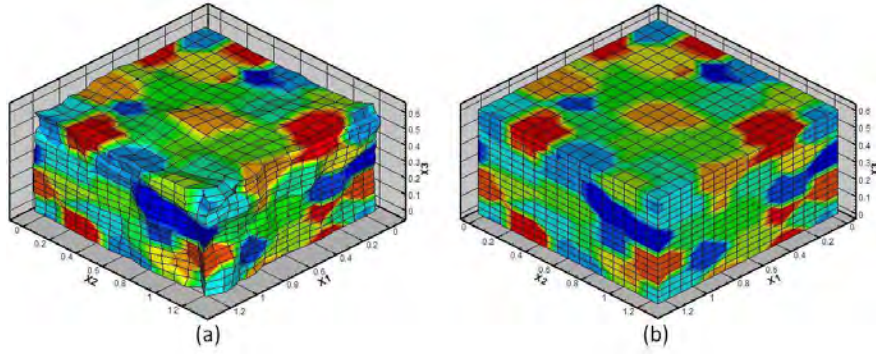


Figure 22: (a) Deformed microstructure predicted by multi-grid CEPFFT. (c) Deformed microstructure predicted by single-grid CEPFFT.

1. The elastic response of the microstructure is successfully captured by CEPFFT. Fatigue properties of nickel-based superalloy microstructures can be efficiently investigated using CEPFFT method. The computed results are comparable with the those based on crystal plasticity finite element simulation.
2. The equilibrium error resulted from the augmented Lagrangian algorithm is comparable with the one resulting from the basic formulation and depends on the resolution of the input image.
3. The CEPFFT model provides consistent prediction of the macroscopic effective mechanical responses and local stress field with the finite element and crystal visco-plasticity fast Fourier transform simulations. The crystallographic texture patterns of microstructures under different deformation modes estimated by the three methods are almost identical.
4. The local strain fields obtained by the CEPFFT implementation agree very well with visco-plastic results and have similar patterns with the crystal plasticity finite element results.
5. The multi-grid strategy that uses separate computation and material grids was shown to successfully capture irregular configuration of deformed microstructures. However, it does not result in significant changes in the mechanical response for the tested examples in comparison to the single-grid method.
6. The required computation time of CEPFFT is significantly less than that of crystal plasticity finite element method since the methodology does not require the solution of any matrix equations as in the FEM.

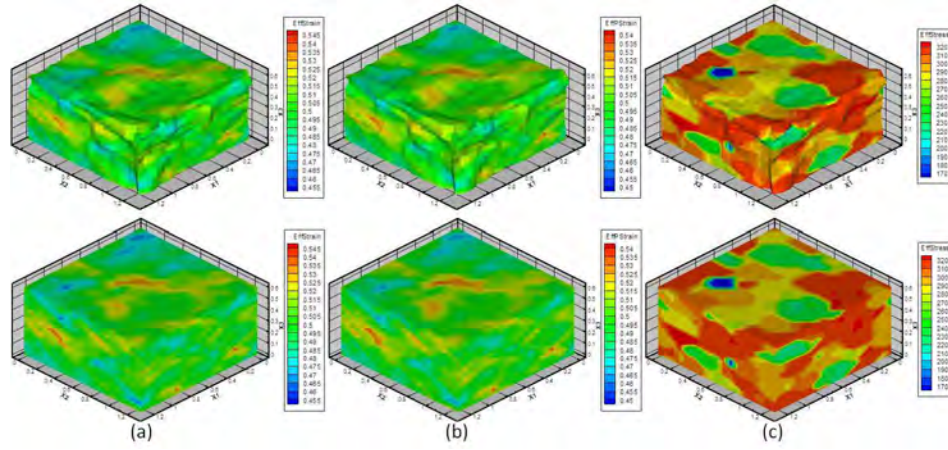


Figure 23: Contour plots of compressed microstructures computed using the multi-grid strategy. The first row shows results obtained from the multi-grid CEPFFT, and the bottom row shows results obtained from the single-grid CEPFFT. (a) Equivalent total strain. (b) Equivalent plastic strain. (c) Equivalent stress.

This computational efficiency provides significant potential in integrating the FFT approach with stochastic multiscale materials simulations.

7. Various CEPFFT can be introduced. The approach highlighted in this paper computes separately the elastic and plastic responses. Careful design of the elasto-plastic modulus for the homogeneous reference medium can improve the computational efficiency.

Acknowledgements

This research was supported by an OSD/AFOSR MURI09 award on uncertainty quantification, the U.S. Department of Energy, Office of Science, Advanced Scientific Computing Research and the Computational Mathematics program of the National Science Foundation (NSF) (award DMS-0809062). This research used resources of the National Energy Research Scientific Computing Center, which is supported by the Office of Science of the U.S. Department of Energy under Contract No. DE-AC02-05CH11231. Additional computing resources were provided by the NSF through TeraGrid resources provided by NCSA under grant number TG-DMS090007.

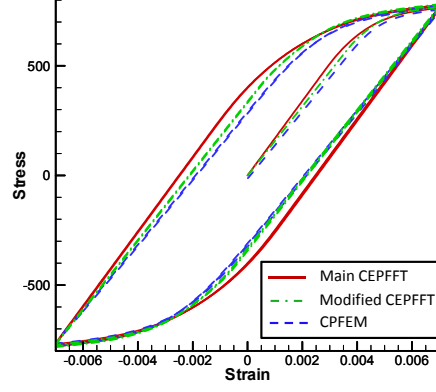


Figure 24: Stress-strain responses of three loops of cyclic loading computed by CEPFFT and CPFEM. Main CEPFFT refers to the main crystal elasto-plasticity FFT method, modified CEPFFT refers to the crystal elasto-plasticity implementation using a homogeneous elasto-plastic medium approach (Remark 2), and CPFEM is the crystal plasticity finite element method.

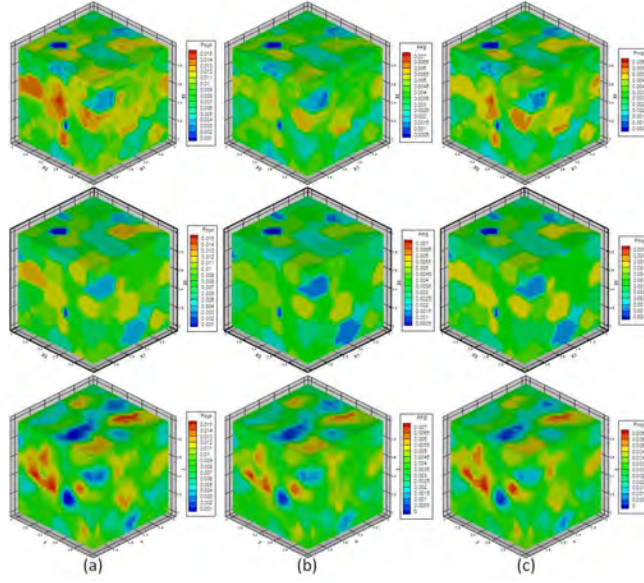


Figure 25: Contour plots of fatigue indicator parameters fields. Main CEPFFT results are placed in the top row, results from the modified CEPFFT formulation (Remark 2) are placed in the middle row, and crystal plasticity finite element results are located in the bottom row. (a) P_{cyc} , (b) P_{FS} , (c) P_{mps} .

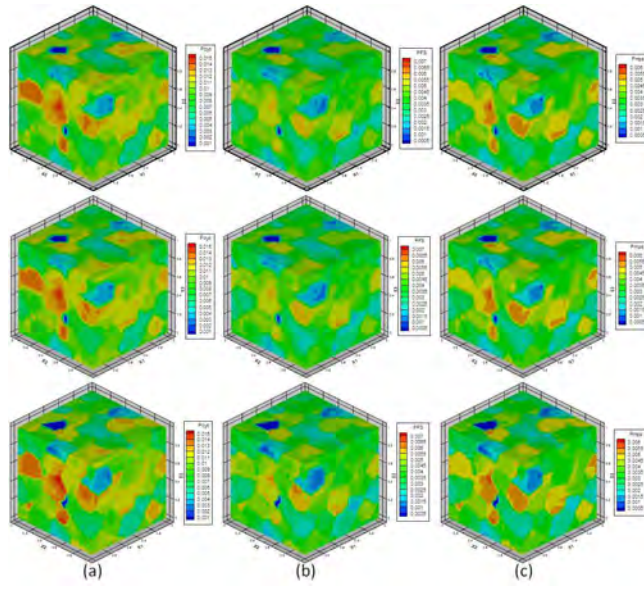


Figure 26: Contour plots of fatigue indicator parameters fields evaluated by the multi-grid CEPFFT on coarse microstructure (top row), single-grid CEPFFT on coarse microstructure (middle row), and single-grid CEPFFT on fine microstructure (bottom row). (a) P_{cyc} , (b) P_{FS} , (c) P_{mps} .

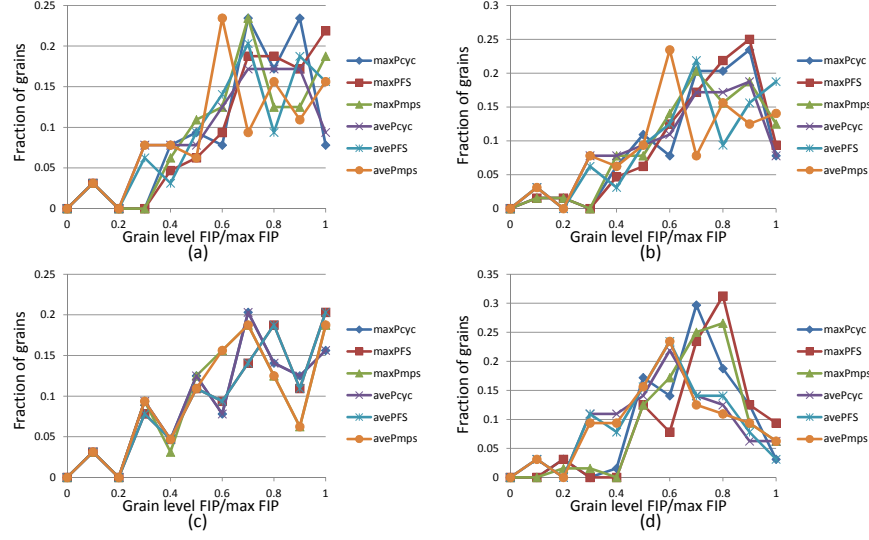


Figure 27: Distribution of the fatigue indicator parameters among grains computed by (a) Main CEPFFT with coarse microstructure, (b) Main CEPFFT with fine microstructure, (c) Modified CEPFFT (Remark 2) with coarse microstructure and (d) crystal plasticity finite element method. These distributions are normalized by the maximum values of each FIP over all grains.

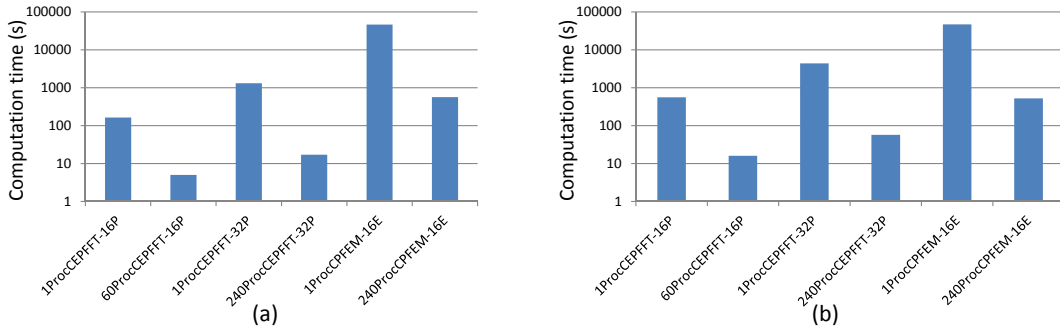


Figure 28: Computation times of simulations using different methods on microstructures with different resolutions. (a) Plane strain deformation to 0.02 strain. (b) One complete loop of cyclic loading on the IN100 microstructure. The computation times are shown in logarithmic scale. In the figure, 1ProcCEPFFT-16P means the CEPFFT simulation of a microstructure discretized by $16 \times 16 \times 16$ voxels using 1 processor and 1ProcCPFEM-16E means the crystal plasticity finite element simulation of a microstructure discretized by $16 \times 16 \times 16$ elements using 1 processor.

References

- [1] G. Sachs, Plasticity problems in metals, *Trans. Faraday Soc.* 24 (1928) 84–92.
- [2] G. Taylor, Plastic strain in metals, *Journal of the Institute of Metals* 62 (1938) 307–324.
- [3] S. Ahzi, R. J. Asaro, D. M. Parks, Application of crystal plasticity theory for mechanically processed bscco superconductors, *Mechanics of Materials* 15 (1993) 201–222.
- [4] T. Lin, Analysis of elastic and plastic strains of a face-centred cubic crystal, *Journal of the Mechanics and Physics of Solids* 5 (1957) 143–149.
- [5] J. W. Hutchinson, Bounds and self-consistent estimates for creep of polycrystalline materials, *Proceedings of the Royal Society of London. A. Mathematical and Physical Sciences* 348 (1976) 101–127.
- [6] R. Asaro, A. Needleman, Overview no. 42 texture development and strain hardening in rate dependent polycrystals, *Acta Metallurgica* 33 (1985) 923–953.
- [7] S. Kalidindi, C. Bronkhorst, L. Anand, Crystallographic texture evolution in bulk deformation processing of fcc metals, *Journal of the Mechanics and Physics of Solids* 40 (1992) 537–569.
- [8] S. R. Kalidindi, Incorporation of deformation twinning in crystal plasticity models, *Journal of the Mechanics and Physics of Solids* 46 (1998) 267–290.
- [9] P. R. Dawson, S. R. MacEwen, P.-D. Wu, Advances in sheet metal forming analyses: dealing with mechanical anisotropy from crystallographic texture, *International Materials Reviews* 48 (2003) 86–122.
- [10] B. Kouchmeshky, N. Zabaras, Modeling the response of hcp polycrystals deforming by slip and twinning using a finite element representation of the orientation space, *Computational Materials Science* 45 (2009) 1043–1051.

- [11] E. Kröner, On the plastic deformation of polycrystals, *Acta Metallurgica* 9 (1961) 155–161.
- [12] J. D. Eshelby, The determination of the elastic field of an ellipsoidal inclusion, and related problems, *Proceedings of the Royal Society of London. Series A, Mathematical and Physical Sciences* 241 (1957) 376–396.
- [13] R. Hill, Continuum micro-mechanics of elastoplastic polycrystals, *Journal of the Mechanics and Physics of Solids* 13 (1965) 89–101.
- [14] J. W. Hutchinson, Elastic-plastic behaviour of polycrystalline metals and composites, *Proceedings of the Royal Society of London. A. Mathematical and Physical Sciences* 319 (1970) 247–272.
- [15] T. Iwakuma, S. Nemat-Nasser, Finite elastic-plastic deformation of polycrystalline metals, *Proceedings of the Royal Society of London. A. Mathematical and Physical Sciences* 394 (1984) 87–119.
- [16] A. Molinari, G. Canova, S. Ahzi, A self consistent approach of the large deformation polycrystal viscoplasticity, *Acta Metallurgica* 35 (1987) 2983–2994.
- [17] R. Lebensohn, C. Tomé, A self-consistent anisotropic approach for the simulation of plastic deformation and texture development of polycrystals: Application to zirconium alloys, *Acta Metallurgica et Materialia* 41 (1993) 2611–2624.
- [18] R. Lebensohn, C. Tomé, A self-consistent viscoplastic model: prediction of rolling textures of anisotropic polycrystals, *Materials Science and Engineering: A* 175 (1994) 71–82. NATO Advanced Research Workshop on Polyphase Polycrystal Plasticity.
- [19] H. Wang, P. Wu, C. Tomé, Y. Huang, A finite strain elastic–viscoplastic self-consistent model for polycrystalline materials, *Journal of the Mechanics and Physics of Solids* 58 (2010) 594–612.
- [20] R. Masson, A. Zaoui, Self-consistent estimates for the rate-dependent elastoplastic behaviour of polycrystalline materials, *Journal of the Mechanics and Physics of Solids* 47 (1999) 1543–1568.

- [21] A. Zaoui, R. Masson, Micromechanics-based modeling of plastic polycrystals: an affine formulation, *Materials Science and Engineering: A* 285 (2000) 418–424.
- [22] P. P. Castañeda, Second-order homogenization estimates for nonlinear composites incorporating field fluctuations: I-theory, *Journal of the Mechanics and Physics of Solids* 50 (2002) 737–757.
- [23] Y. Liu, P. P. Castañeda, Second-order theory for the effective behavior and field fluctuations in viscoplastic polycrystals, *Journal of the Mechanics and Physics of Solids* 52 (2004) 467–495.
- [24] R. A. Lebensohn, C. N. Tomé, P. P. Castañeda, Self-consistent modelling of the mechanical behaviour of viscoplastic polycrystals incorporating intragranular field fluctuations, *Philosophical Magazine* 87 (2007) 4287–4322.
- [25] D. Peirce, R. Asaro, A. Needleman, An analysis of nonuniform and localized deformation in ductile single crystals, *Acta Metallurgica* 30 (1982) 1087–1119.
- [26] F. Roters, P. Eisenlohr, L. Hantcherli, D. Tjahjanto, T. Bieler, D. Raabe, Overview of constitutive laws, kinematics, homogenization and multi-scale methods in crystal plasticity finite-element modeling: Theory, experiments, applications, *Acta Materialia* 58 (2010) 1152–1211.
- [27] L. Anand, M. Kothari, A computational procedure for rate-independent crystal plasticity, *Journal of the Mechanics and Physics of Solids* 44 (1996) 525–558.
- [28] A. Acharya, A. Beaudoin, Grain-size effect in viscoplastic polycrystals at moderate strains, *Journal of the Mechanics and Physics of Solids* 48 (2000) 2213–2230.
- [29] W. Li, N. Zabaras, A virtual environment for the interrogation of 3d polycrystalline microstructures including grain size effects, *Computational Materials Science* 44 (2009) 1163–1177.
- [30] C. P. Przybyla, D. L. McDowell, Microstructure-sensitive extreme value probabilities for high cycle fatigue of Ni-base superalloy IN100, *International Journal of Plasticity* 26 (2010) 372–394.

- [31] B. Wen, N. Zabaras, Investigating variability of fatigue indicator parameters of two-phase nickel-based superalloy microstructures, *Computational Materials Science* 51 (2012) 455–481.
- [32] R. Lebensohn, N-site modeling of a 3D viscoplastic polycrystal using Fast Fourier Transform, *Acta Materialia* 49 (2001) 2723–2737.
- [33] R. Lebensohn, P. Ponte Castañeda, R. Brenner, O. Castelnau, Full-field vs. homogenization methods to predict microstructure-property relationships of polycrystalline materials, in: S. Ghosh, D. Dimiduk (Eds.), *Computational Methods for Microstructure-Property Relationships*, Springer, 2011, pp. 393–441.
- [34] H. Moulinec, P. Suquet, A fast numerical method for computing the linear and nonlinear mechanical properties of composites, *Comptes rendus de l’Académie des sciences. Série II, Mécanique, Physique, Chimie, Astronomie* 318 (1994) 1417–1423.
- [35] H. Moulinec, P. Suquet, A numerical method for computing the overall response of nonlinear composites with complex microstructure, *Computer Methods in Applied Mechanics and Engineering* 157 (1998) 69–94.
- [36] J. C. Michel, H. Moulinec, P. Suquet, A Computational Method Based on Augmented Lagrangians and Fast Fourier Transforms for Composites with High Contrast, *CMES-Computer Modeling in Engineering & Sciences* 1 (2000) 79–88.
- [37] R. Lebensohn, O. Castelnau, R. Brenner, P. Gilormini, Study of the antiplane deformation of linear 2-d polycrystals with different microstructures, *International Journal of Solids and Structures* 42 (2005) 5441–5459.
- [38] R. A. Lebensohn, R. Brenner, O. Castelnau, A. D. Rollett, Orientation image-based micromechanical modelling of subgrain texture evolution in polycrystalline copper, *Acta Materialia* 56 (2008) 3914–3926.
- [39] R. A. Lebensohn, Y. Liu, P. P. Castañeda, Macroscopic properties and field fluctuations in model power-law polycrystals: full-field solutions versus self-consistent estimates, *Proceedings of the Royal Society of London. Series A: Mathematical, Physical and Engineering Sciences* 460 (2004) 1381–1405.

- [40] A. Prakash, R. A. Lebensohn, Simulation of micromechanical behavior of polycrystals: finite elements versus fast fourier transforms, *Modelling and Simulation in Materials Science and Engineering* 17 (2009) 064010.
- [41] B. Liu, D. Raabe, F. Roters, P. Eisenlohr, R. A. Lebensohn, Comparison of finite element and fast fourier transform crystal plasticity solvers for texture prediction, *Modelling and Simulation in Materials Science and Engineering* 18 (2010) 085005.
- [42] S.-J. Kim, D. H. Kim, K. H. Oh, A. D. Rollett, R. A. Lebensohn, H. N. Han, An elastoplastic finite element modeling coupled with orientation image based micromechanical approach, *AIP Conference Proceedings* 1252 (2010) 103–106.
- [43] N. Lahellec, J. Michel, H. Moulinec, P. Suquet, Analysis of inhomogeneous materials at large strains using fast Fourier transforms, in: C. Miehe (Ed.), *IUTAM symposium on computational mechanics of solids materials*, Kluwer Academic, Stuttgart, Germany, 2001, pp. 247–268.
- [44] M. Shenoy, J. Zhang, D. McDowell, Estimating fatigue sensitivity to polycrystalline ni-base superalloy microstructures using a computational approach, *Fatigue & Fracture of Engineering Materials & Structures* 30 (2007) 889–904.
- [45] M. Shenoy, Y. Tjiptowidjojo, D. McDowell, Microstructure-sensitive modeling of polycrystalline IN 100, *International Journal of Plasticity* 24 (2008) 1694–1730. Special Issue in Honor of Jean-Louis Chaboche.
- [46] S. Sankaran, N. Zabaras, Computing property variability of polycrystals induced by grain size and orientation uncertainties, *Acta Materialia* 55 (2007) 2279–2290.
- [47] M. Frigo, S. Johnson, The design and implementation of FFTW3, *Proceedings of the IEEE* 93 (2005) 216–231.
- [48] D. Sulsky, Z. Chen, H. Schreyer, A particle method for history-dependent materials, *Computer Methods in Applied Mechanics and Engineering* 118 (1994) 179 – 196.

- [49] D. Sulsky, S.-J. Zhou, H. L. Schreyer, Application of a particle-in-cell method to solid mechanics, *Computer Physics Communications* 87 (1995) 236 – 252. Particle Simulation Methods.
- [50] D. McDowell, F. Dunne, Microstructure-sensitive computational modeling of fatigue crack formation, *International Journal of Fatigue* 32 (2010) 1521–1542.
- [51] P. Suquet, personal communication, 2011.
- [52] S. R. Kalidindi, H. K. Duvvuru, Spectral methods for capturing crystallographic texture evolution during large plastic strains in metals, *Acta Materialia* 53 (2005) 3613–3623.
- [53] S. R. Kalidindi, H. K. Duvvuru, M. Knezevic, Spectral calibration of crystal plasticity models, *Acta Materialia* 54 (2006) 1795–1804.
- [54] M. Knezevic, S. R. Kalidindi, D. Fullwood, Computationally efficient database and spectral interpolation for fully plastic taylor-type crystal plasticity calculations of face-centered cubic polycrystals, *International Journal of Plasticity* 24 (2008) 1264–1276.
- [55] M. Knezevic, H. F. Al-Harbi, S. R. Kalidindi, Crystal plasticity simulations using discrete fourier transforms, *Acta Materialia* 57 (2009) 1777–1784.